

REMOTE DETECTION OF HYDROGEN LEAK USING Nd:YAG PULSED LASER
INDUCED DUAL LINE DETECTION RAYLEIGH LIGHT SCATTERING

By

VENKATA SURYA RAGHURAM VEMPATI

A THESIS PRESENTED TO THE GRADUATE SCHOOL
OF THE UNIVERSITY OF FLORIDA IN PARTIAL FULFILLMENT
OF THE REQUIREMENTS FOR THE DEGREE OF
MASTER OF SCIENCE

UNIVERSITY OF FLORIDA

2005

Copyright 2005

by

Venkata Surya Raghuram Vempati

ACKNOWLEDGMENTS

I would like to thank Dr. Jill Peterson for her support and guidance. I would also like to thank my fellow students (Sameer Paranjpe, Philip Jackson, Murray Fisher, Mathew Gabriel and Ryan Ferguson) for their assistance in various portions of the project.

TABLE OF CONTENTS

	<u>page</u>
ACKNOWLEDGMENTS	iii
LIST OF TABLES	vi
LIST OF FIGURES	vii
LIST OF ABBREVIATIONS AND SYMBOLS.....	x
ABSTRACT.....	xiv
CHAPTER	
1 INTRODUCTION.....	1
Project Goal	1
Rayleigh Light Scattering.....	1
2 LITERATURE SURVEY.....	4
3 THEORETICAL BACKGROUND.....	6
Light Scattering	6
Mechanism of Elastic Scattering.....	7
Mie scattering.....	8
Rayleigh scattering.....	10
Angular scattering cross-section	12
Dual Line-detection Technique	13
Buoyant Jets and Plumes	15
4 EXPERIMENTAL METHODS AND APPARATUS	17
Gas-flow Path.....	20
Varying Glare	20
Design of Plate Position.....	20
Experimental Methods.....	31
Integrated Area Method.....	31
Peak Voltage Method	33
Peak Area Correlation	35

5	RESULTS AND DISCUSSION.....	37
	Numerical Results.....	37
	Experimental Results.....	38
	Testing the Linearity of the Photomultiplier-tube Output Voltage	38
	Eliminating Glare from the Rayleigh Light Scattering Signal	42
	Reference value method	42
	Assuming that the ratio of the glare at the two wavelengths is constant	43
	Theoretical and Experimental Photon-arrival Rates.....	45
	Theoretical photon-arrival rate.....	45
	Experimental photon-arrival rate	46
	Analysis of the Recorded Data	48
	Raw photomultiplier-tube voltage variation	48
	Variation of glare as a function of radial and plate position	52
	Variation of Rayleigh light scattering signal as a function of radial and plate position.....	53
	Detection limits	56
	Correlation studies.....	59
6	CONCLUSIONS AND RECOMMENDATIONS	61
	LIST OF REFERENCES.....	63
	BIOGRAPHICAL SKETCH	65

LIST OF TABLES

<u>Table</u>	<u>page</u>
4-1 Percent variation in average peak voltage for 355 and 532 nm	35
5-1 Optical density and the corresponding transmission of neutral density filters.....	41
5-2 Photomultiplier-tube voltages before and after using the 0.6 neutral density filter.	42
5-3 Scattering cross-sections of helium, nitrogen, hydrogen and air at 532 nm and 355 nm.....	46

LIST OF FIGURES

<u>Figure</u>	<u>page</u>
3-1 Raman Scattering	7
3-2 Creation of an induced dipole moment by an electric field	8
3-3 Mie scattering geometry	9
3-4 Rayleigh scatterer is very small compared to the wavelength of the incident electromagnetic wave.....	11
3-5 Instantaneous and time averaged profiles of a typical buoyant jet	16
4-1 Experimental setup used for collection of scattered light at 90°	17
4-2 Mounting of nozzle, gas-flow meters and position of aluminum plate	18
4-3 Collecting lens of radius R_C and having focal point at (0,0).	22
4-4 Ray tracing of the reflected rays from the aluminum plate at the collecting lens.	23
4-5 Ray tracing of the reflected rays from the collecting lens at the focusing lens	24
4-6 Solid angle subtended by the reflected rays from the aluminum plate	25
4-7 Ray tracing output from MATLAB when the aluminum plate is directly over the nozzle	27
4-8 Ray tracing output from MATLAB when the aluminum plate is 3 cm from the nozzle.	28
4-9 Ray tracing output from MATLAB when the aluminum plate is 7 cm from the nozzle.	29
4-10 Glare for different plate positions as a function of number of rays.	29
4-11 Glare as a function of plate position and wavelength.....	30
4-12 Typical waveform from a photomultiplier tube.....	31
4-13 Running average of area	32

4-14	Percent variation in area.....	33
4-15	Running average of peak voltage.....	33
4-16	Percent variation in peak voltage.....	34
4-17	Correlation between peak voltage and area	35
5-1	Signal-to-glare ratio as a function of plate position.....	37
5-2	Comparison of experimental and theoretical glare	38
5-3	Photomultiplier-tube and the photodiode voltage as a function of the power meter voltage.....	39
5-4	Photomultiplier-tube voltage as a function of the power meter voltage when the glare is varied using an aluminum plate.	40
5-5	Theoretical photon-arrival rates.....	46
5-6	Comparisons of theoretical and experimental photon-arrival rates	47
5-7	Percent error between theoretical and experimental photon-arrival rates	48
5-8	Raw Photomultiplier-tube voltages as a function of radial and plate position for 532 nm	49
5-9	Raw Photomultiplier-tube voltages as a function of radial and plate position for 355 nm.	51
5-10	Percentage errors in raw Photomultiplier-tube voltage for two typical plate positions as a function of radial position.	51
5-11	Glare as a function of radial and plate position for 532 nm.....	52
5-12	Glare as a function of radial and plate position for 355 nm.....	53
5-13	Rayleigh light scattering signal as a function of radial and plate position for 532 nm	54
5-14	Rayleigh light scattering signal as a function of radial and plate position for 355 nm	55
5-15	Signal-to-glare as a function of radial and plate position for 532 nm and 355 nm.....	56
5-16	Raw Photomultiplier-tube voltages as a function of radial and plate position for 532 nm and 355 nm.....	57

5-17	Rayleigh light scattering signal as a function of radial and plate position for 532 nm	58
5-18	Rayleigh light scattering signal as a function of radial and plate position for 355 nm	58
5-19	Correlation of Rayleigh light scattering signal between two wavelengths.....	59
5-20	Variation in R^2 value as a function of plate position.....	60

LIST OF ABBREVIATIONS AND SYMBOLS

<u>Symbol</u>	<u>Description</u>
a	Particle radius (m)
A^*	Area of the back ground surface visible to the detector(m^2)
A	Area under the voltage time curve
c	Speed of light (m/s)
C	Optical system calibration constant
C^*	Surface scattering parameter
C_{PMT}	Photomultiplier tube calibration constant
dV	Control volume (m^3)
d_p	Diameter of Rayleigh scattering particle
e	Electronic charge = $1.602E-19$ Coulombs
E_1, E_2, E_3	Energy states of a molecule.
\vec{E}	Electric field vector
\vec{B}	Magnetic field vector
\vec{S}	Scattering field
h	Planck's constant = $6.626E-34$ Js
I	Intensity (photons/ m^2 -pulse)
I_0	Incident laser power (photons/ m^2 -pulse)
k	Boltzmann constant (Joule/Kelvin)

n	Refractive index of the gas
\bar{n}	Number of moles
N	Molecular number density (molecules/m ³)
N^*	Number of molecules
N_A	Avogadro's number
P	Pressure (N/m ²)
r	Radial distance from jet centerline (m)
r_{pl}	Distance between the collecting lens and the aluminum plate
Re	Reynolds number = $\rho vD / \mu$
\bar{R}	Universal gas constant (8.314 J/ mol K)
R	Ratio of the reflectivity at 532 nm and 355 nm
R_C	Radius of the collecting lens (m)
R_p	Photon arrival rate (photons/m ² -pulse)
S	Ratio of the scattering cross-sections at 532nm and 355 nm
T	Temperature of gas Kelvin)
v	Velocity of buoyant jet (m/s)
V	Photomultiplier tube voltage (V)
x	Percentage of leaking fluid (80% nitrogen and 20% helium) in the control volume.
z	Downstream distance (mm)

Greek Symbols

α	Size parameter = $2\pi a/\lambda$
β	Spread angle

θ	Angle of observation measured from the forward to scattering directions.
ϕ	Scattering angle
ψ	Wave function
η	Optical efficiency of transmitting and collecting lenses
ϖ	Uncertainty
$d\omega$	Solid angle of the collection optics
λ	Wavelength of laser light (nm)
σ	Scattering cross-section (m ²)
ρ	Reflectivity
∇	Volume (m ³)
μ	Dynamic viscosity of gas (Pa-s)
ν	Frequency (Hz)
Δt	Time interval between two readings(s)

Subscripts

$\lambda 1$	532 nm wavelength line
$\lambda 2$	355 nm wavelength line
a	Ambient
act	Actual
air	Air
avg	Average
<i>Collectinglens</i>	Intensity of the reflected light at the collecting lens
<i>FWHM</i>	Full width half maximum

Focusing	Lens intensity of light at focusing lens
<i>Glare</i>	Scattering intensity due to Glare
i	Species
inc	Incident
leak	Scattering intensity due to leaking fluid(80% nitrogen and 20% helium)
min	Minimum
max	Maximum
Mie Scattering	Mie scattering
PMT	Intensity of light at the photomultiplier tube
r1	Energy state 1
r2	Energy state 2
<i>Rayleigh</i>	Rayleigh
<i>reflected</i>	Intensity of the reflected light
<i>RLS</i>	Rayleigh light scattering
ref	Reference condition
<i>scat</i>	Scattering

Abstract of Thesis Presented to the Graduate School
of the University of Florida in Partial Fulfillment of the
Requirements for the Degree of Master of Science

REMOTE DETECTION OF HYDROGEN LEAK USING Nd:YAG PULSED LASER
INDUCED DUAL LINE DETECTION RAYLEIGH LIGHT SCATTERING

By

Venkata Surya Raghuram Vempati

May 2005

Chair: Jill Peterson

Major Department: Mechanical and Aerospace Engineering

Our primary objective was to use laser induced Rayleigh light scattering to detect the presence of hydrogen leaks in the presence of high amounts of glare. A mathematical code in MATLAB was written to design the glare system and to compute the glare numerically. Experimental and numerical results corresponded well with a maximum error of 5%. Pure helium and a mixture of 20% helium and 80% nitrogen were used to simulate the hydrogen leak. The mixture of helium and nitrogen is used because the scattering cross-section of the mixture of 20% helium and 80% nitrogen is equal to that of hydrogen. The scattering cross-section of helium was 0.015 times that of air and the scattering cross-section of hydrogen was 0.23 times that of air. Major problems in using the Rayleigh light scattering as a diagnostic tool are uncertainty due to electronic shot noise and glare from the background surfaces. The uncertainty due to electronic shot noise was found to be less than 0.1% for an averaging time of 0.001 sec. The Nd:YAG pulsed laser (operating at wavelengths of 532 nm and 355 nm) was used. Intensity of the

scattered light due to the helium and nitrogen molecules in the jet was measured using a photomultiplier tube. Data were acquired using a high-speed digital oscilloscope. An aluminum plate was used to vary the glare. The ratio of the minimum to the maximum intensity of scattering light was 0.2 when a mixture of helium and nitrogen was used (for measurements at a downstream distance of 4 nozzle diameters). When pure helium was used (for measurements at a downstream distance of 8 nozzle diameters) the ratio of the minimum to the maximum intensity of scattered light was 0.14. It was possible to detect the hydrogen leak even with glare-to-signal ratios as high as 6:1.

CHAPTER 1 INTRODUCTION

Project Goal

We designed and tested an experimental setup to measure hydrogen leaks in a buoyant jet in the presence of high amounts of glare or low signal-to-glare ratios. We used an Nd: YAG pulsed laser induced dual line-detection Rayleigh light-scattering technique to eliminate the glare.

Rayleigh Light Scattering

Rayleigh scattering is an attractive technique for non-intrusive measurements with high spatial and temporal resolution of gas-flow properties (such as density, temperature, concentration in a mixture of gases and velocity in the case of high-speed flows). All of these experiments measured the intensity of the scattered Rayleigh light to determine the property of interest. All of these applications required a laser beam passing through the gas. The laser beam is elastically scattered by the gas molecules when the incident electromagnetic wave reacts with the dipoles in the gas molecules and the light beam is scattered in all directions. Rayleigh light scattering is easy to set up compared to other scattering techniques (such as Raman scattering). The main difficulty of Raman scattering is the low scattered signal intensity, which requires relatively long integration times for adequate signal-to-noise ratios and requires very low background-flame radiation. The Rayleigh scattering cross-section is about 1000 times larger than the vibrational Raman scattering resulting in much larger intensity

Two commonly encountered difficulties associated with Rayleigh scattering are the contamination of the scattered signal with background noise and scattering from particulates present in the gas (which is known as Mie scattering). Background noise comes from two sources: the surface-scattered laser glare; and the light from the test environment (which usually is broad band). Because the Rayleigh scattered light from the control volume is at the same frequency and wavelength as the laser beam, it is difficult to discriminate the surface scattered light from the Rayleigh signal. This problem is intensified when measurements are taken in closed enclosures. Glare can be controlled principally by blackening the surfaces.

Our study used a dual line-detection technique to address the problem the background noise. We used an Nd: YAG pulse laser with a repetition rate of 10Hz. The signal was collected at two laser lines of wavelengths 532 nm and 355 nm with the energy of the laser being 200 mJ/pulse and 60-95 mJ/pulse at 532 nm and 355 nm respectively. Using the pulse laser provides a high level of Rayleigh signal because of the high energy densities at each pulse. The signal obtained from the two lines is analyzed simultaneously to eliminate the glare from the Rayleigh signal. The dual line-detection technique greatly enhances the scope of the Rayleigh scattering technique as a measurement tool since it completely eliminates background noise from the Rayleigh signal; thus improving the Rayleigh signal. The system was tested and calibrated at various levels of background noise. Finally, measurements were taken using a mixture of helium and nitrogen issuing out of a nozzle. Changes in concentration were measured by traversing the nozzle in the radial direction (to and from the centerline); thereby changing the concentration of gas due to entrainment of air. Results indicate that accurate

measurements are possible with the dual-line-detection technique in the presence of high levels of background glare. Our work is the first step towards the remote detection of hydrogen leaks.

CHAPTER 2 LITERATURE SURVEY

Lord Rayleigh was the first person to systematically observe light scattering, in 1871. The basics of Rayleigh and Mie scattering theory have been described (Van De Hulst, 1957, Kerker, 1969, Bohren and Huffman 1983). They gave the general solution of the Maxwell equations that describes independent scattering of incident electromagnetic waves by an isolated sphere. The solution is termed Mie scattering theory; and is a complicated series solution. For particles that are small compared to the wavelength of the incident light ($r \leq 0.03\lambda$), the Mie series simplifies; and is termed Rayleigh scattering. The initial term in the series is dominant and is sufficient to express the intensity of the scattered light. McCartney (1976) gave a good description of Rayleigh light scattering.

Laser-induced Rayleigh light scattering has been used for many purposes in the past. It has been used successfully for temperature measurements (Pitz et al. 1976; Dibble, Hollenbach and Rambach 1980; Bill et al. 1981). Pitts and Kashiwagi (1984) used Rayleigh light scattering to study turbulent mixing. (Namer and Scheffer, 1985; Namazina, 1989) used Rayleigh light scattering for combustion studies. Rayleigh light scattering has also been used to obtain temperature measurements in heated buoyant jet (Otugen and Namer (1988)). Otugen (1993) used a dual line-detection technique to simultaneously determine the glare and remove it from the Rayleigh signal of interest. Pitts, and Bryner, (1992) used Rayleigh scattering for investigation of free jets and

plumes. It has also been used for temperature measurements in rapid thermal chemical vapor deposition reactor by J.E. Peterson and J.F.Horton, (1998).

CHAPTER 3 THEORETICAL BACKGROUND

Light Scattering

Scattering is a process by which a particle in the path of an electromagnetic wave continuously abstracts energy from the incident wave and reradiates that energy into the total solid angle centered at that particle. For scattering to occur it is necessary that the refractive index of the particle be different from the surrounding medium.

There are two types of light scattering mechanisms: elastic scattering and inelastic scattering. Inelastic scattering is also called Raman scattering and in this type of scattering the frequency of the scattered wave is different from that of the incident wave and there is a change in the energy of the incident wave. The molecule may either gain energy from, or lose energy to, the photon. In Figure 3.1, 3 energy states of the molecule are shown (E_1 , E_2 , and E_3). The molecule is originally at the E_2 energy state. The photon interacts with the molecule, exciting it with an energy $h\nu_{inc}$. However, there is no stable state of the molecule corresponding to this energy, and so the molecule relaxes down to one of the energy levels shown. In doing this, it emits a photon.

If the molecule relaxes to energy state E_1 , it will have lost energy, and so the photon emitted will have energy $h\nu_{r1}$, where $h\nu_{r1} > h\nu_{inc}$. These transitions are known as anti-Stokes transitions. If the molecule relaxes to energy state E_3 , it will have gained energy, and so the photon emitted will have energy $h\nu_{r2}$, where $h\nu_{r2} < h\nu_{inc}$. These transitions are known as Stokes transitions.

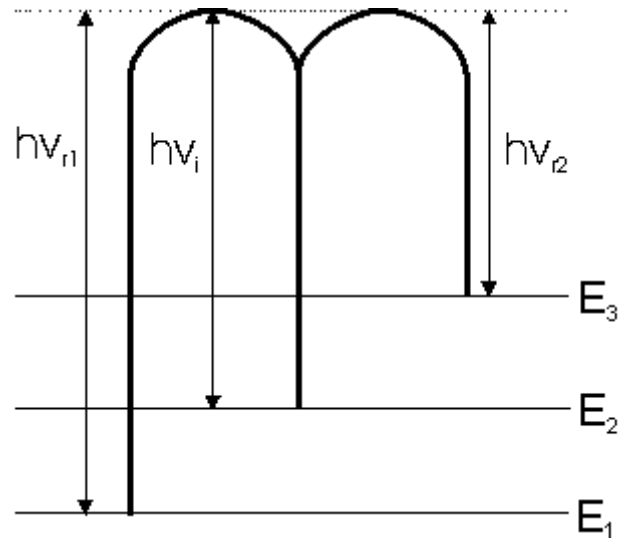


Figure 3-1. Raman scattering

Mechanism of Elastic Scattering

Consider an elemental scatterer such as a gas molecule in the path of an electromagnetic wave. The gas molecule can be considered as a mechanical oscillator of unequal masses carrying opposite charges at the center and the periphery according to McCartney (1976). The elastic scattering theory assumes that the molecule is isotropic, non polar and non-ionized. These assumptions mean that the molecule does not experience a net force in an electric field and the negative charge is uniformly distributed at the periphery and may be treated as though it were at the center. This means there is a negative charge at the center with equal positive charge. Hence the net dipole moment, which is equal to the product of the charge and the separation distance, is equal to zero. But when the molecule is subjected to external electric field of an electromagnetic wave, the charges are forced apart (Figure 3-2) and an induced dipole moment is created. This induced dipole moment oscillates synchronously with the field and emits a secondary wave with the same frequency as that of the incident electromagnetic wave and this secondary wave is the scattered wave. An oscillating dipole emits electromagnetic waves

because it contains oscillating electric currents, and because the changing positions of the positive and negative charges make it harder for their electric effects to cancel. This elastic scattering of light can be explained by using two theories.

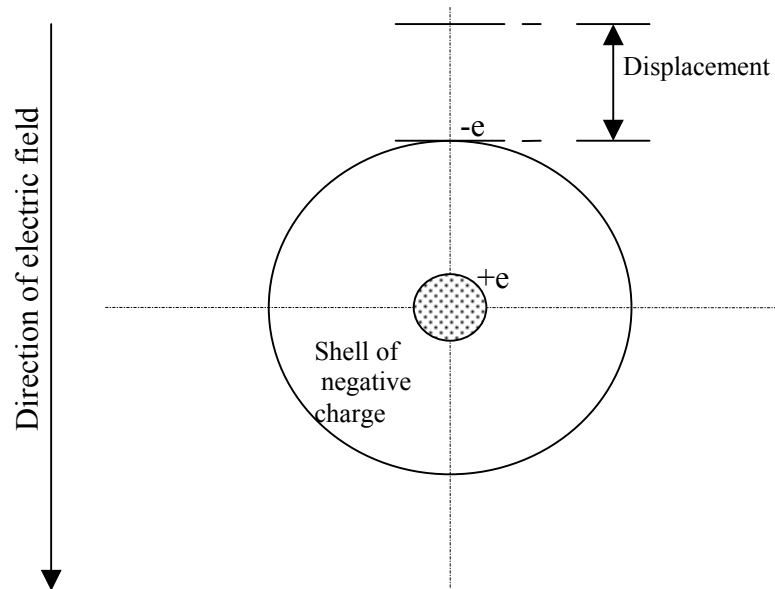


Figure 3-2. Creation of an induced dipole moment by an electric field which displaces the plus and minus charges of the molecule. (Source: McCartney, Earl J., *Optics of the Atmosphere*, 1976, Figure 4.2, pp. 179-181, New York, John Wiley & Sons.)

Mie scattering

Scattering by particles of arbitrary size is called Mie scattering and is discussed in detail by Kerker (1969). Starting with very small particles, as the particle size relative to the wavelength increases, there is a gradual transition from Rayleigh to Mie scattering, which is characterized by

- A complicated dependence of scattered light intensity on the angle of observation, the complexity increasing with particle size relative to wavelength.
- An increasing ratio of forwarding scattering to backscattering as the particle size increases.
- Little dependence of scattering on wavelength when particle size relative to wavelength is large.

Mie scattering has no size limitations and converges to the limits of geometrical optics for large particles. Mie theory may therefore be used for describing most spherical particle scattering systems (including Rayleigh scattering). However, Rayleigh scattering theory is preferred if applicable, due to the complexity of the Mie scattering theory. The criteria for Rayleigh scattering is $\alpha \ll 1$, where α is the dimensionless size parameter given by Equation 3-1, where a is the spherical particle radius, and λ is the scattering wavelength

$$\alpha = \frac{2\pi a}{\lambda}, \quad (3-1)$$

Figure 3-3 shows the spherical coordinate scattering geometry used for Mie light scattering for light incident on a single particle. Using this coordinate system, the scattering parameters may be defined as follows.

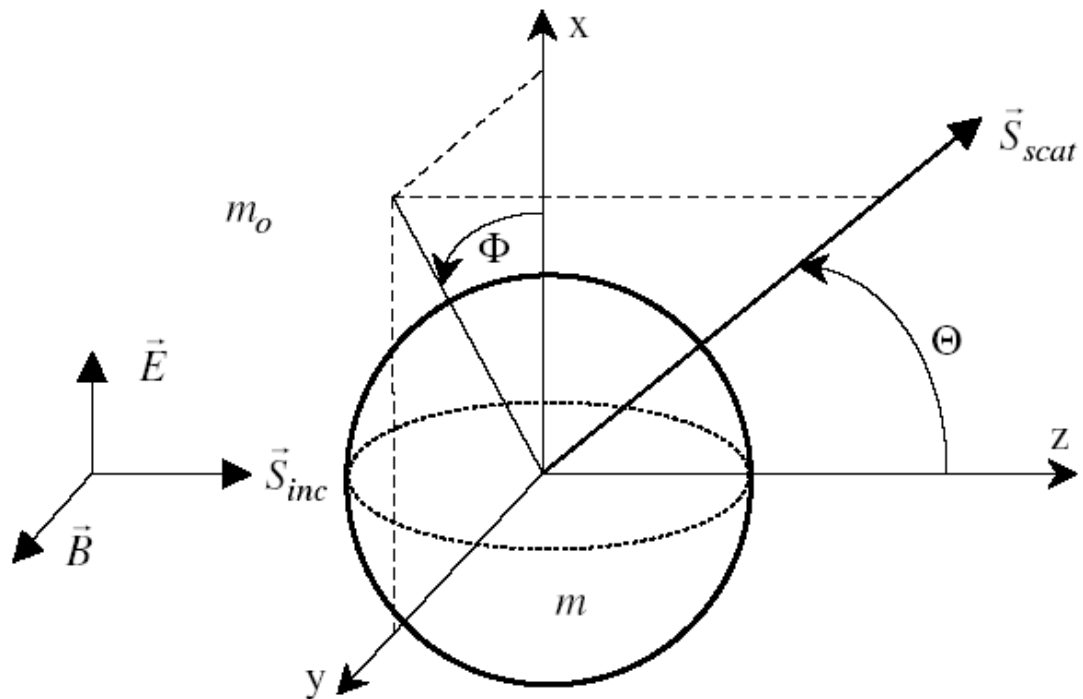


Figure 3-3. Mie Scattering Geometry. (Source: <http://plaza.ufl.edu/dwhahn/Light%20Scattering%20Theory.pdf>, Last accessed December 5th, 2004).

For each scattering angle (ϕ, θ) , the Equations (3-2) and (3-3) represent the intensities of scattered radiation vertically and horizontally polarized with respect to the scattering plane, which is defined by the incident and scattered ray,

$$I_{\phi} = I_o \frac{\lambda^2}{4\pi^2 r^2} i_1 \sin^2 \phi \quad (3-2)$$

$$I_{\theta} = I_o \frac{\lambda^2}{4\pi^2 r^2} i_2 \cos^2 \phi \quad (3-3)$$

In this formulation, I_o is the incident intensity, and the intensity functions i_1 and i_2 given by Equations 3-4 and 3-5.

$$i_1 = \left| \sum_{n=1}^{\infty} \frac{2n+1}{n(n+1)} [a_n \pi_n(\cos \theta) + b_n \tau_n(\cos \theta)] \right|^2 \quad (3-4)$$

$$i_2 = \left| \sum_{n=1}^{\infty} \frac{2n+1}{n(n+1)} [a_n \tau_n(\cos \theta) + b_n \pi_n(\cos \theta)] \right|^2 \quad (3-5)$$

Where π_n and τ_n are the angular dependent functions and are expressed in terms of Legendre polynomials by

$$\pi_n(\cos \theta) = \frac{P_n^{(1)}(\cos \theta)}{\sin \theta} \quad (3-6)$$

$$\tau_n(\cos \theta) = \frac{dP_n^{(1)}(\cos \theta)}{d\theta} \quad (3-7)$$

The constants a_n and b_n are obtained from the boundary conditions that the tangential components of the electric field and magnetic field of the incident wave are continuous over the entire surface of the sphere.

Rayleigh scattering

The Mie solution is a complex mathematical solution and for particles of size much less than the wavelength of the incident light, the Mie solution converges in one term and

is called Rayleigh theory and is discussed in detail by McCartney (1976). Rayleigh scattering is elastic scattering of an electromagnetic wave by particles far smaller than the wavelength of the incident wave (Figure 3-4). The electromagnetic radiation is scattered in all directions different than that of the incoming light.

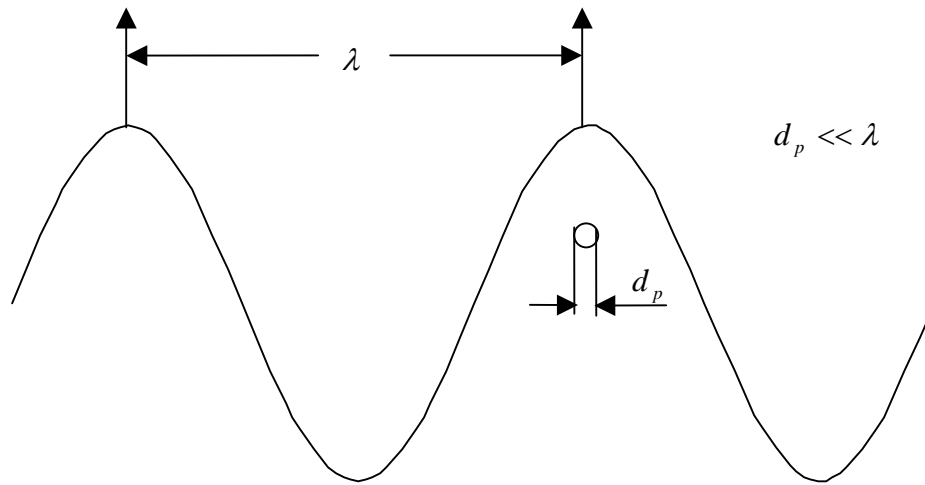


Figure 3-4. The size of a Rayleigh scatterer is very small as compared to the wavelength of the incident electromagnetic wave

Lord Rayleigh assumed that the particles were spherical, isotropic, far smaller than the wavelength of light, and denser than the surrounding medium. He showed through simple reasoning that the scattering varies as the square of the particle volume and inversely as the fourth power of wavelength of light.

Rayleigh scattering is marked by several characteristics:

- The amount of light scattered varies nearly as the inverse fourth power of the wavelength.
- Spatial distribution of scattered light bears a simple relationship to the direction of observation.
- The light scattered at 90 degrees is almost completely polarized.

In the domain of light scattering, the concepts of angular and total scattering cross-sections are basic concepts. These concepts lead to several coefficients and expressions having great practical utility.

Angular scattering cross-section

The angular scattering cross-section of a molecule is defined as that cross-section of an incident wave, acted on by the molecule, having an area such that the power flowing across it is equal to the power scattered by the molecule per steradian.

The angular scattering cross-section represents the ratio of the scattered intensity to the incident irradiance.

$$\sigma(90^\circ) = \frac{4\pi^2 (n-1)^2}{N^2 \lambda^4} \quad (3-8)$$

This expression is derived for an ideal gas assuming that $n-1 \ll 1$. The refractive index term, $n-1$, is proportional to the molecular number density. Therefore, the scattering cross-section for an individual molecule is not a function of N , and is independent of gas temperature, pressure and density.

For a volume of gas, however, the amount of scattered light is proportional to gas number density. The random spacing and thermal motion of gas molecules are such that scattering is incoherent and independent. The result is that there are no discernable phase relationships between the separately fluxes except in the exact forward direction and thus the individual intensities are additive. The scattered intensity is therefore, is directly proportional to the molecular number density.

$$I(90^\circ)_{scat} = \sigma(90^\circ)NI_o \quad (3-9)$$

The constant of proportionality is defined by the solid angle of the collection optics, the length of the control volume and the optical efficiency of the collection optics.

Hence the intensity of the Rayleigh scattered light from a control volume containing a mixture of gases is given by

$$I_{RLS} = I_o(d\omega)(dV)(\eta) \sum (N\sigma)_i \quad (3-10)$$

Dual Line-detection Technique

The major problem in using Rayleigh light scattering as a diagnostic tool is background glare and Mie scattering. Mie scattering due to dust and aerosols can be reduced by filtering the incoming air. To eliminate the glare from the Rayleigh signal, dual line-detection technique is used in this project. It involves obtaining the scattered light intensity using two different lines of the laser and solving the set of simultaneous linear equations to eliminate the glare from the Rayleigh signal. It is known that the Rayleigh signal is proportional to the incident laser intensity and the gas number density and also to the scattering cross-section, where C is the optical system calibration constant and N is the gas number density.

$$I(90^\circ)_{RLS} = C\sigma(90^\circ)NI_o \quad (3-11)$$

The gas number density is the ratio of the number of molecules to the volume occupied by them. It can be written mathematically as

$$N = \frac{\text{number of molecules}}{\text{Volume occupied by the molecules}} = \frac{N^*}{V} \quad (3-12)$$

$$\text{Where } N^* = (\text{number of moles})(\text{Avogadros's Number}) = \bar{n} * N_A \quad (3-13)$$

From the ideal gas law it can be noted that the gas number density can be replaced by the pressure, temperature and Boltzmann constant. The ideal gas law is given by Equation 3-14, where \bar{n} is the number of moles and \bar{R} is the universal gas constant (8.3145 J/mol K).

$$P\forall = \overline{\overline{nRT}}, \quad (3-14)$$

Replacing \overline{n} with gas number density in Equation 3-14, ideal gas law can be written as

$$P = NkT, \quad (3-15)$$

Where k is Boltzmann constant and is defined as

$$k = \frac{\overline{R}}{N_A} = 1.38066\text{E-}23 \text{ J/K} \quad (3-16)$$

$$N_A = \text{Avogadro's number} = 6.023\text{E}23$$

Hence the intensity of the Rayleigh signal can be written as

$$I_{RLS} = C \frac{P}{kT} I_o \sigma \quad (3-17)$$

The scattered light intensity detected by the photomultiplier-tube is the sum of the Rayleigh signal and the glare. Hence the intensity of the scattered light incident on the photomultiplier-tube can be written as

$$I_{scat} = I_{RLS} + I_{Glare} \quad (3-18)$$

I_{Glare} is proportional to the incident intensity and the reflection from the background surfaces.

$$I_{Glare} = C^* I_o \rho A_{Lens} \quad (3-19)$$

Where C^* is the surface scattering parameter and A^* is the area of the background surface visible to the detector. Hence the scattered light intensity can be written as

$$I_{scat} = (CI_o \frac{P}{kT} \sigma) + (C^* I_o \rho A_{Lens}) \quad (3-20)$$

The scattered intensity can be normalized with the incident intensity to account for the pulse to pulse variation in the incident intensity of the laser. Hence the scattered light intensity can be written as

$$\frac{I_{scat}}{I_0} = C \frac{P}{kT} \sigma + C^* \rho A_{Lens} \quad (3-21)$$

Since two different lines of wavelengths 532 nm and 355 nm are used, the intensity of the scattered light at both these wavelengths can be written as

$$\left(\frac{I_{scat}}{I_o} \right)_{\lambda 1} = C_{\lambda 1} \frac{P}{kT} \sigma_1 + C^*_{\lambda 1} \rho_{\lambda 1} A_{Lens} \quad (3-22)$$

$$\left(\frac{I_{scat}}{I_o} \right)_{\lambda 2} = C_{\lambda 2} \frac{P}{kT} \sigma_2 + C^*_{\lambda 2} \rho_{\lambda 2} A_{Lens} \quad (3-23)$$

Hence by varying either the pressure, temperature or the scattering cross-section individually or a combination of any of the three parameters, the intensity of the scattered light can be obtained at different conditions and then by solving the simultaneous set of equations using linear regression the glare can be eliminated from the Rayleigh signal.

The detailed description of how the glare is eliminated is given in Chapter 5

Buoyant Jets and Plumes

The primary objective in this project is to detect a hydrogen leak. For this purpose a mixture of helium and nitrogen are used that issue out of a nozzle and since the densities of both helium and nitrogen are different from the surrounding ambient air, buoyancy forces arise in the jet.

A fluid motion is called a jet if its primary source of kinetic energy and momentum flux is a pressure drop through an orifice. A fluid motion whose primary source of kinetic energy and momentum flux is body forces is called a plume and flows whose motion is in transition from a jet to plume are called forced plume or a buoyant jet.

For a jet, due to conservation of momentum, the momentum flux is constant along the jet axis. Since the mass flux increases along the jet axis due to entrainment, the axial

velocity must correspondingly decrease. For a plume, the buoyant force tends to accelerate the fluid in the plume in a vertical direction, turning the plume axis in the direction of the buoyant force. For a plume initially discharged upwards, and with an upwards buoyancy force, the deceleration (caused by entrainment) is hence less than for the case of a jet. Figure 3-5 shows the instantaneous and time averaged profiles of a buoyant jet.

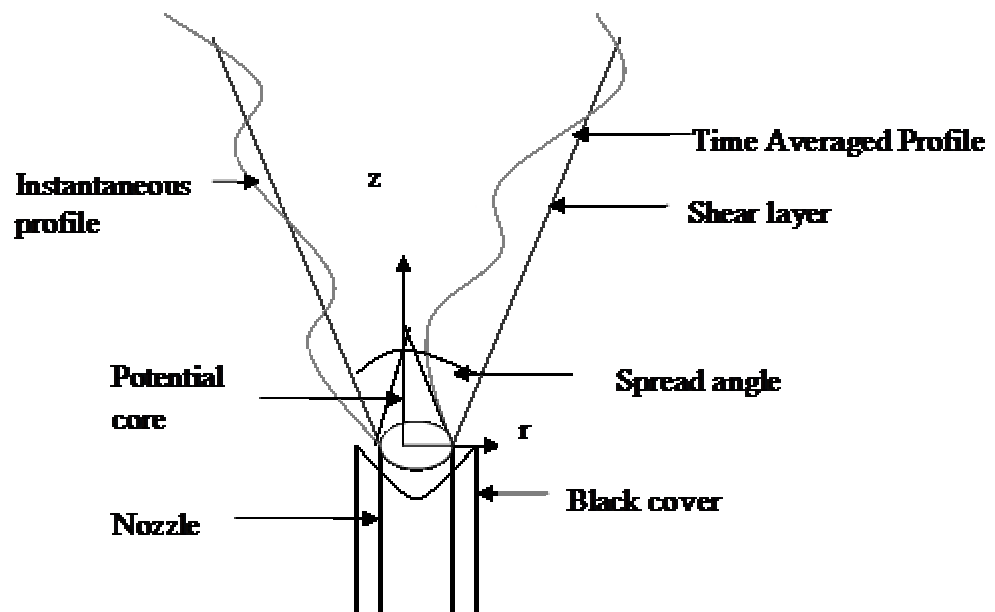


Figure 3-5. Instantaneous and time averaged profiles of a typical buoyant jet

Inside the potential core the concentration of the flow fluid is 100% and at the edge of the shear layer the concentration of the flow fluid is 0%. According to Chen and Rodi (1980) the spread angle is 13° for vertical round buoyant jet.

CHAPTER 4 EXPERIMENTAL METHODS AND APPARATUS

This chapter describes the design of experimental set up for detecting the hydrogen leaks by measuring the intensity of the scattered light at 90 degrees to the incident light. The leak was simulated using a jet of pure helium in some cases and a mixture of 20% helium and 80% nitrogen in others. The mixture of 20% helium and 80% nitrogen was used because the scattering cross-section of the mixture is equal to the scattering cross-section of hydrogen which is $1.89\text{E-}32 \text{ m}^2/\text{sr}$. at 532 nm. Also, the data acquisition system used to measure the intensity is described.

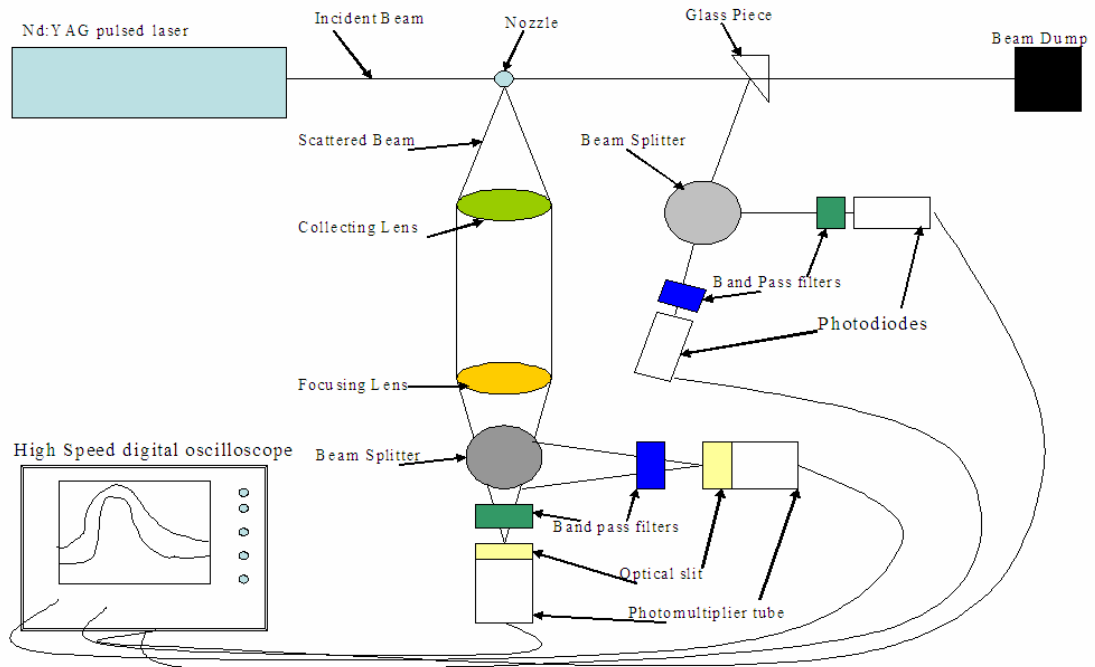


Figure 4-1. A schematic of experimental setup used for collection of scattered light at 90°

The incident laser beam was generated by an Nd:YAG pulsed laser, the fundamental wavelength being 1064 nm and the energy being 450 mJ/pulse at that

wavelength. However in our work, the laser was operated at 532 nm and 355 nm wavelengths using 2nd and 3rd harmonic generators. The energy of the laser was 200 mJ/pulse and 60-95 mJ/pulse at 532 nm and 355 nm respectively. The laser was operated at a frequency of 10 Hz and the pulse width of the beam was 10 ns with a beam diameter of 6 mm and a beam divergence of 1.1°. The incident laser beam passed over the jet of helium coming through a nozzle.

A ¼” diameter nozzle was used to simulate the leak, it was placed at a distance of 10” from the laser and hence the diameter of the laser beam at the nozzle is 8 mm. The leak was simulated at a Reynolds number of 100. The nozzle was mounted on 3 micrometer traverses for 3-dimensional motion (Figure 4-2)

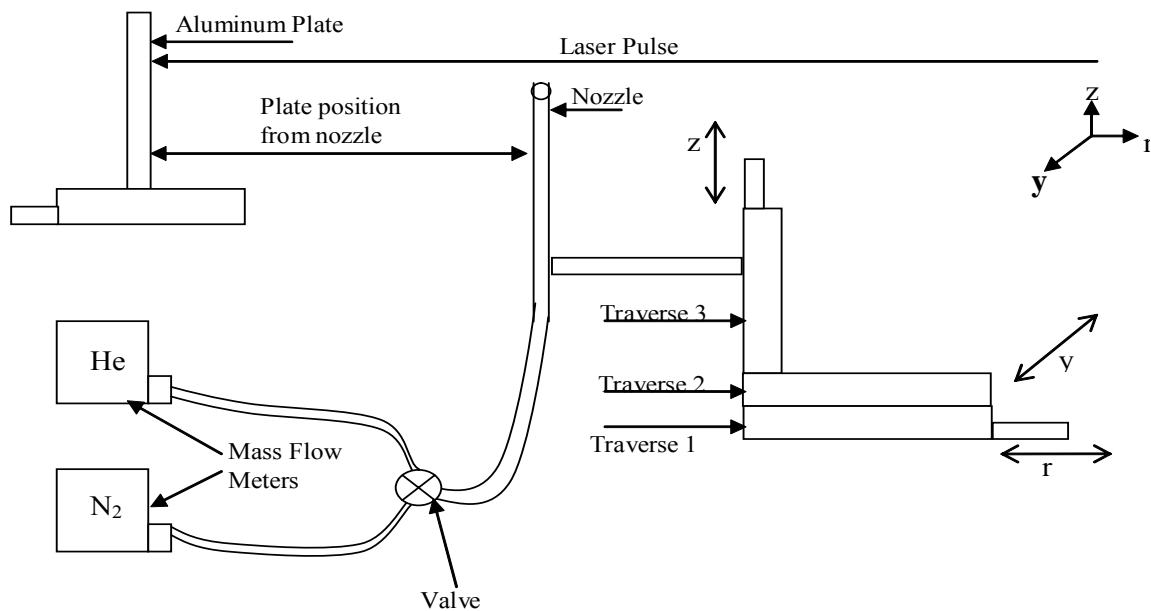


Figure 4-2. Mounting of nozzle, gas-flow meters and position of aluminum plate

The least count of each traverse was 0.05 mm. The mass flow rate of pure helium and the mixture of helium and nitrogen were monitored using the mass flow controllers. When no plate was used, the laser beam was trapped using a beam dump which was placed at a distance of 20” from the nozzle.

The collection optics were oriented at 90 degrees to the incident laser beam (Figure 4-1) and consisted of a pair of 60 mm diameter lenses.(from TSI optics). The collecting lens has a focal length of 254 mm and this lens collects and collimates the scattered and reflected light. The focusing lens has a focal length of 124 mm and this lens focuses the collimated beam onto a 0.15 mm and 3 mm long slit which was mounted on the face of the photomultiplier-tube. The scattered light was separated into two different lines of wavelengths 532 nm and 355 nm using a beam splitter (from CVI lasers.) The beam splitter had a manufacturer coated transmissivity of 100% at 355 nm and 100% reflectivity at 532 nm. Band pass filters (from Newport) were mounted in front of both the photomultiplier tubes which allow only the respective wavelengths to pass through and eliminated any light of other wavelengths to be detected by the photomultiplier-tubes. The collection optics and the two photomultiplier-tubes were covered with a black drape to reduce any stray light to be detected by the photomultiplier-tubes.

The photomultiplier-tube was Hamamatsu model HC120-01 and has a built in amplifier with adjustable gain. The spectral range of the photomultiplier-tube was 185 to 650 nm and has a frequency response of 23 kHz. The signal from the photomultiplier-tube was acquired using a high-speed digital oscilloscope.

The oscilloscope is a LeCroy model LT 372. It was triggered externally using the pulsed-laser. The laser sends a trigger pulse to the oscilloscope exactly 100 ns before pulsing and after 100 ns the laser sends an output beam. The oscilloscope was set to record the data 100 ns after it received the trigger pulse. The signal from the two photomultiplier-tubes was acquired on two different channels of the oscilloscope.

A portion of the incident laser beam was deflected using a piece of glass and was focused onto two different photodiodes (from Thor Labs) with the aid of a beam splitter to monitor the pulse-to-pulse variation in the incident beam power. The signal from the two photodiodes was analyzed using two different channels on a high-speed digital oscilloscope. A band pass filter was mounted in front of each photodiode to eliminate any light other than the signal at the respective wavelengths to be detected by the two photodiodes.

Gas-flow Path

The leak was simulated using a mixture of 20% helium and 80% nitrogen coming out of a nozzle. The gases used were pressurized in high pressure cylinders. The gases from these cylinders were connected to the nozzle using hoses and the mass flow rate was monitored using two gas-flow meters.

Varying Glare

To vary the glare an aluminum plate was used (Figure 4.2). The laser beam was reflected from the aluminum plate and the intensity of the reflected light was measured by the two photomultiplier-tubes. The plate was mounted directly in the line of the incident beam on a traverse so that it can be traversed in the horizontal direction (to and fro from the center of the control volume) and thus the glare could be varied.

Design of Plate Position

To calculate the glare numerically and to study how the glare varies as a function of the plate position, a ray tracing program was written in MATLAB. The rays were traced from the surface of the aluminum plate to the collecting lens, focusing lens and finally onto the photomultiplier tube. The code used simple co-ordinate geometry and Snell's law to trace the rays

Snell's law states the ratio of the sine of the angle a particular kind of wave makes in one medium to the sine of the angle it makes in another medium is a constant. This constant is also called the index of refraction. It can be represented in mathematical form as

$$n_A \sin \theta_A = n_B \sin \theta_B \quad (4-1)$$

The assumptions made in the numerical design of plate position are

- The light reflected from the aluminum plate was 100% diffuse.
- All calculations were made in 2-dimensional plane.
- The pulse-to-pulse variations in the incident laser beam were neglected.
- The reflectivity of aluminum plate is assumed to be 0.93 at 532 nm and 0.85 at 355 nm.
- The number of rays used to calculate glare ranged from 100 to 100000
- The glare computed numerically was glare from the plate only and the glare from the background surfaces was neglected.

The collecting lens was drawn using the general equation of the circle (Equation 4.2) with the focal point of the lens as the center and the radius of the collecting lens as the radius of the circle (Figure 4-3).

$$x^2 + y^2 = R_C^2 \quad (4-2)$$

Only a fraction of the rays reflected from the aluminum plate reached the collecting lens. To trace the rays from the collecting lens to the focusing lens, Snell's law was applied at both ends of the collecting lens (Equation 4-1). The reflected rays from the aluminum plate incident on the collecting lens bend toward the normal \hat{n}_A (Figure 4-4) as the refractive index of the lens is greater than the refractive index of air. The normal

\hat{n}_A to the collecting lens at (p_1, q_1) is perpendicular to the flat surface of the collecting lens.

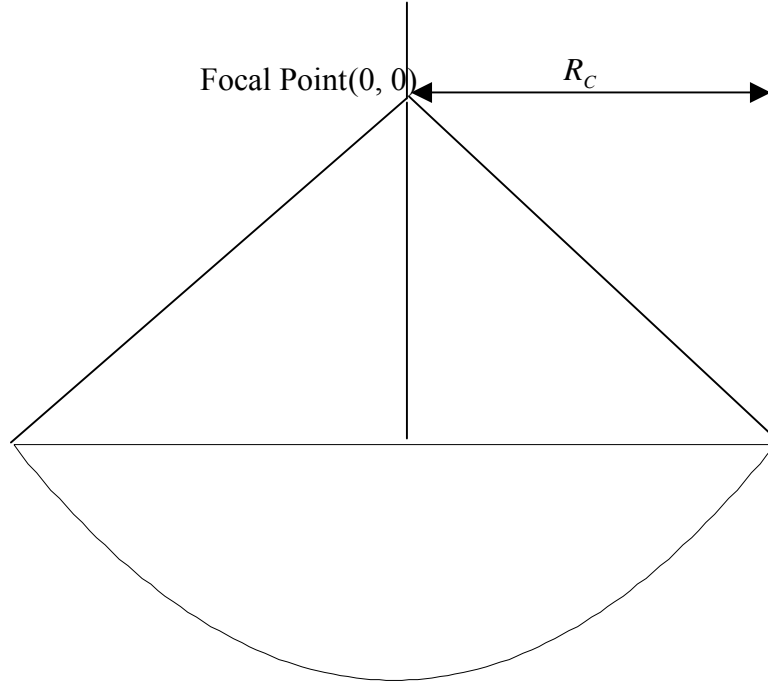


Figure 4-3. Collecting lens of radius R_C and having focal point at $(0,0)$.

The angle of incidence is θ_A and the angle of reflectance is θ_B . The refractive index of air is 1.0029 and that of the collecting lens is 1.523.

The angle of incidence of the reflected rays at the second edge of the collecting lens is θ_C and the angle of reflectance is θ_D . The rays exiting the collecting lens bend away from the normal \hat{n}_B (Figure 4-4). The normal \hat{n}_B to the collecting lens is drawn by differentiating the Equation 4-2 at (p_2, q_2) as given by the Equation 4-3. The transmitted rays from the collecting lens are incident on the curved surface of the focusing lens with an angle of incidence of θ_E and have an angle of reflectance of θ_F .

$$\hat{n}_B = \frac{-1}{(dy/dx)_{(p_2, q_2)}} \quad (4-3)$$

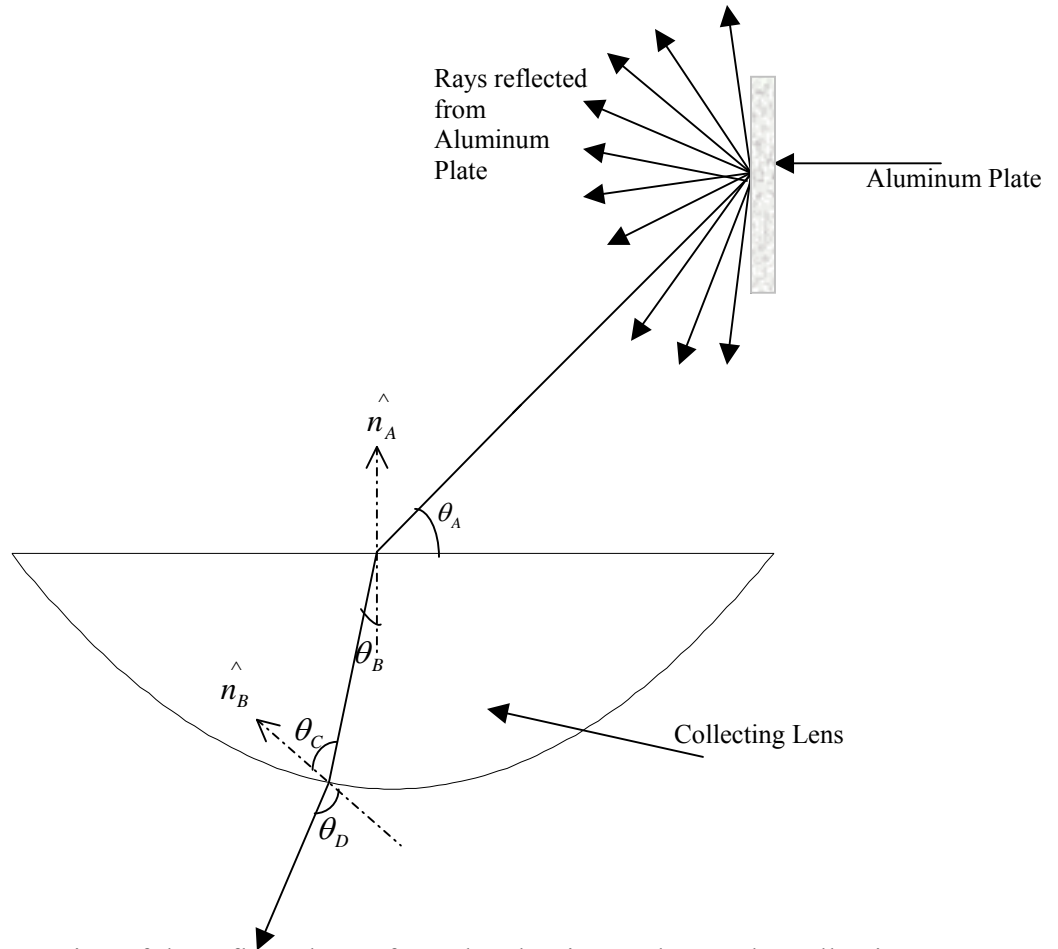


Figure 4-4. Ray tracing of the reflected rays from the aluminum plate at the collecting lens

To trace the rays from the focusing lens to the photomultiplier-tube, Snell's law was applied at both ends of the focusing lens (Equation 4-1). The ray's incident on the focusing lens from the collecting lens bend toward the normal \hat{n}_C and the rays exiting the focusing lens will bend away from the normal \hat{n}_D (Figure 4-5). The intensity of the light reflected from the aluminum plate was calculated given by Equation 4-4. As mentioned in the assumptions, 100000 rays were used in the calculation of the glare and each individual ray was assumed to have equal intensity because the rays were reflected diffusely from the aluminum plate.

$$I_{\text{reflected}} = I_o \rho \quad (4-4)$$

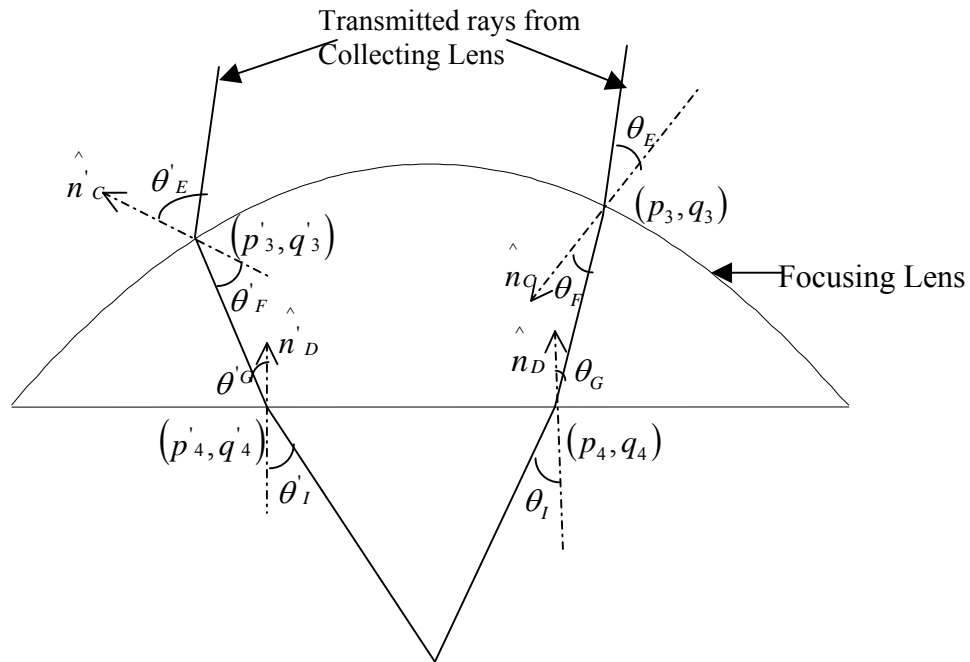


Figure 4-5. Ray tracing of the reflected rays from the collecting lens at the focusing lens

The intensity of the reflected light at the collecting lens was calculated based on number of rays reaching the collecting lens from the aluminum plate and since each ray has equal intensity, the total intensity is the product of number of rays and the intensity of individual ray

The incident laser light was assumed to be diffusely reflected in all directions. Only a fraction of the reflected rays reached the collecting lens which was calculated by computing the solid angle subtended by the reflected rays at the collecting lens. The solid angle $d\omega$ subtended by a surface is defined as the surface area of a unit sphere covered by the surface's projection onto the sphere. The solid angle was calculated according to the formula given by Equation 4-5, where r_{pl} is the radius of the hemisphere which is the

distance between the aluminum plate and the collecting lens (Figure 4-6), and R_C is the radius of the collecting lens

$$d\omega = \frac{\text{projected area of the collecting lens}}{\text{Area of the Hemisphere of radius } r_{pl}} = \frac{\pi R_C^2 \cos \theta}{\pi r_{pl}^2} \quad (4-5)$$

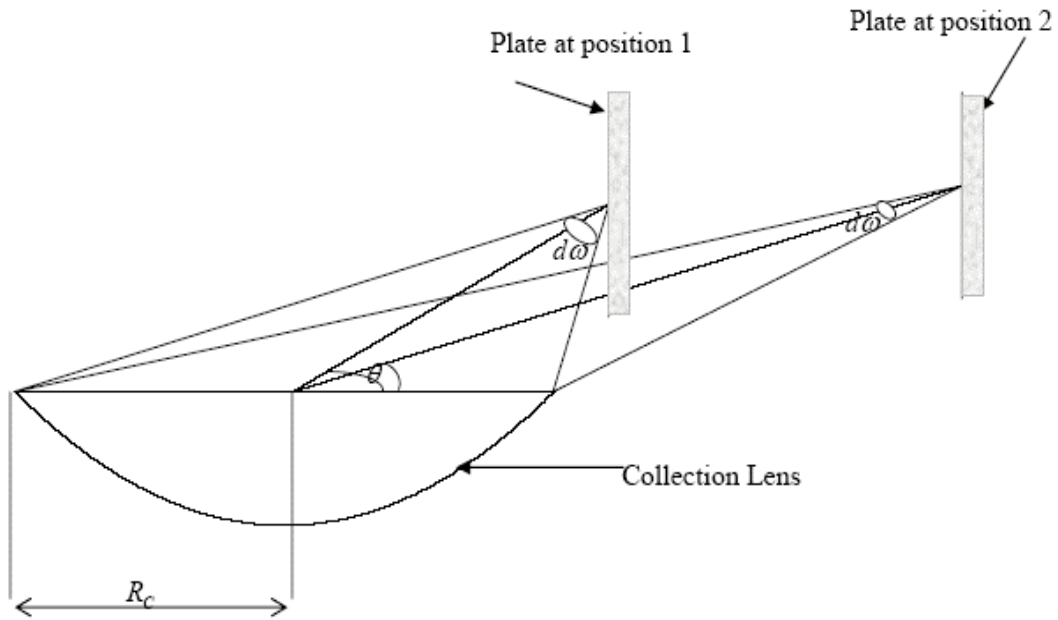


Figure 4-6. Solid angle subtended by the reflected rays from the aluminum plate at the collecting lens for two different plate positions.

The intensity of the reflected light at the collecting lens is given by Equation 4-6.

$$I_{\text{collecting lens}} = (I_{\text{reflected}}) (d\omega) \quad (4-6)$$

Then the intensity of the reflected light at the focusing lens is calculated based on the number of rays reaching the focusing lens from the collecting lens (Equation 4-7), where the term 0.9 is the optical efficiency of the collecting lens.

$$I_{\text{focusing lens}} = (I_{\text{collecting lens}}) (0.9) \left(\frac{\text{number of rays reaching the focusing lens}}{\text{total number of rays}} \right) \quad (4-7)$$

The intensity of the reflected light at the photomultiplier tube is calculated based on the number of rays reaching the photomultiplier tube from the focusing lens (Equation 4-8), where 0.9 is the optical efficiency of the focusing lens.

$$I_{PMT} = (I_{focusing\ lens})(0.9) \left(\frac{\text{number of rays reaching the PMT}}{\text{total number of rays}} \right) \quad (4-8)$$

Figure 4-7 shows the output of the MATLAB code for the case where the aluminum plate was directly over the nozzle. As the focal point of the collecting lens was at the nozzle, the reflected rays from the aluminum plate originated at the focal point of the collecting lens and were collimated. The collimated beam from the collecting lens was focused by the focusing lens onto the photomultiplier-tube. The photomultiplier-tube was at the focal point of the focusing lens.

Figure 4-8 shows the output from the MATLAB code for the case when the aluminum plate was 3 cm from the nozzle. Not all the rays reflected by the collecting lens reached the focusing lens.

Figure 4-9 shows the output from the MATLAB code for the case when the aluminum plate was 7 cm from the nozzle. It was observed that none of the rays reflected by the collecting lens reached the focusing lens and the glare from the aluminum plate detected by the photomultiplier-tube was zero for this case.

Figure 4-10 shows the signal-to-glare as a function of number of rays used in the code. 100 to 100000 rays are used in the computation of the glare. Using more than 100000 rays was time consuming and the results obtained were not significantly accurate as compared to the results obtained with 100000 rays. The x-axis in the figure is the plate position in meters from the control volume. Theoretical Rayleigh scattered signal was used for the computing the signal-to-glare ratio.

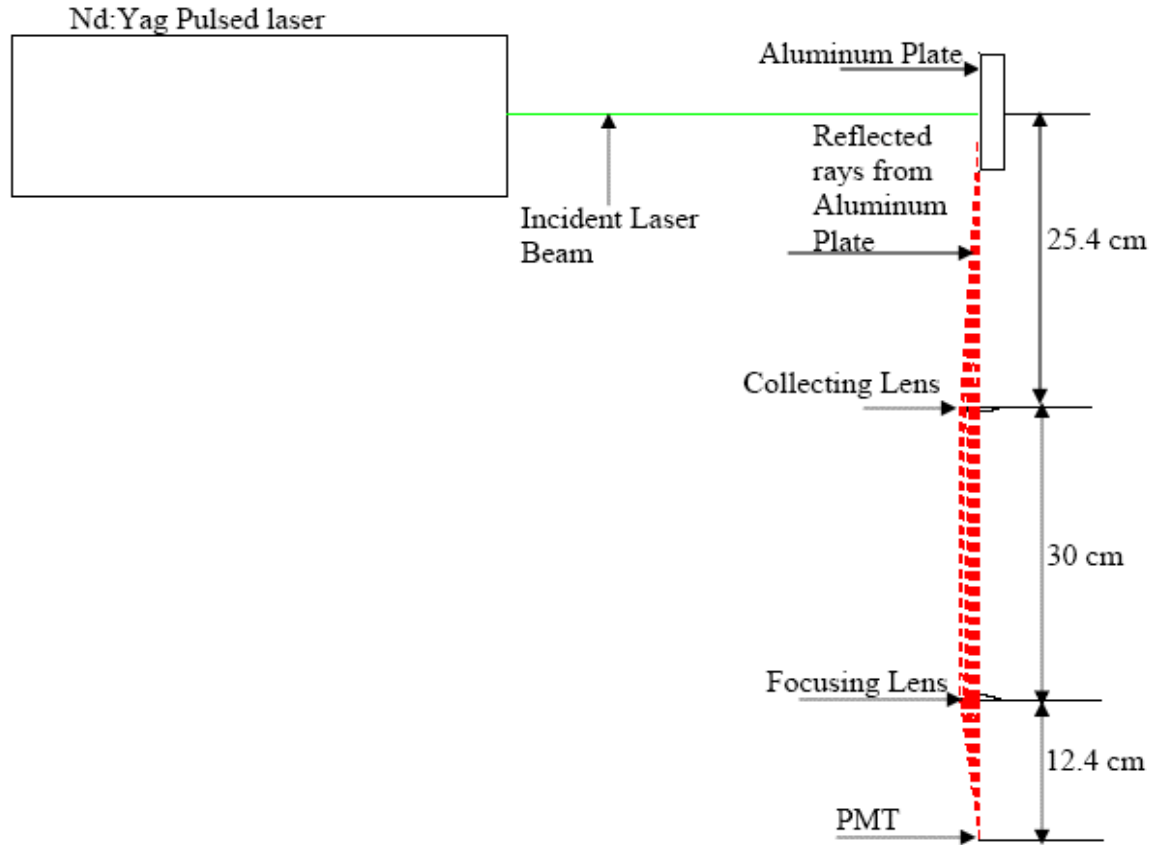


Figure 4-7. Ray tracing output from MATLAB when the aluminum plate is directly over the nozzle

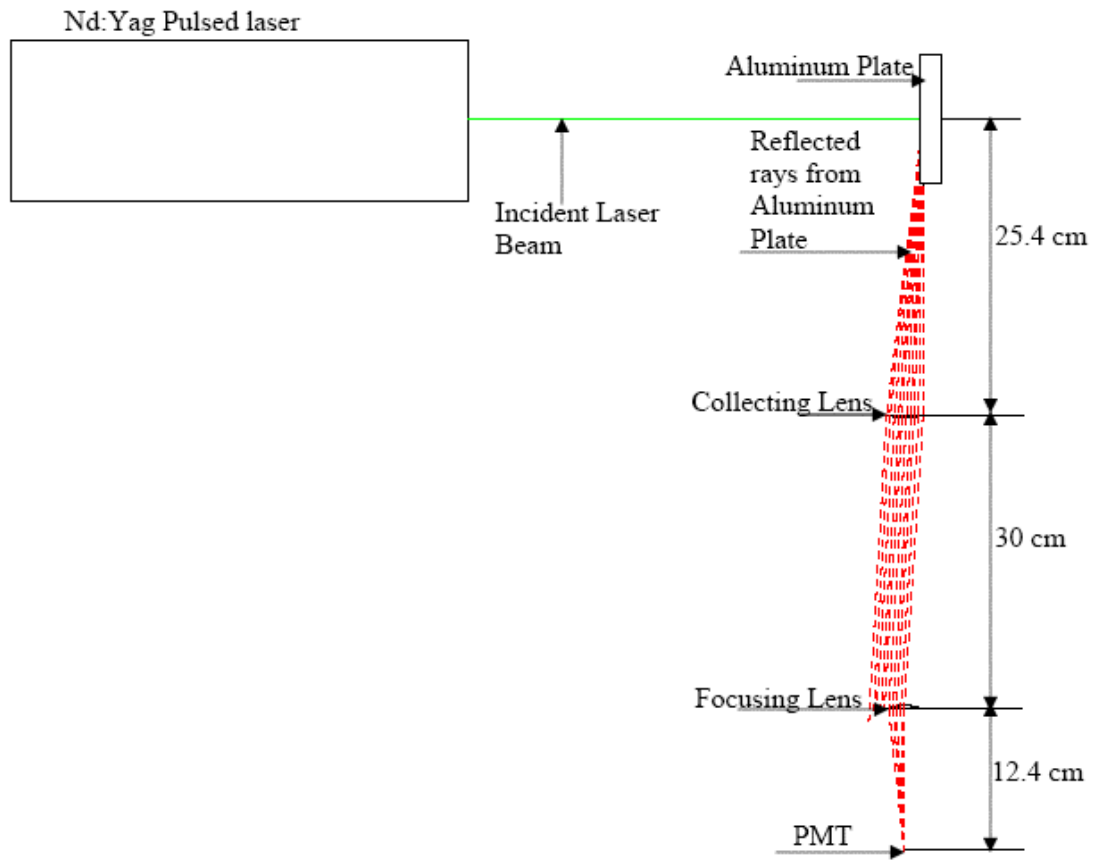


Figure 4-8. Ray tracing output from MATLAB when the aluminum plate is 3 cm from the nozzle.

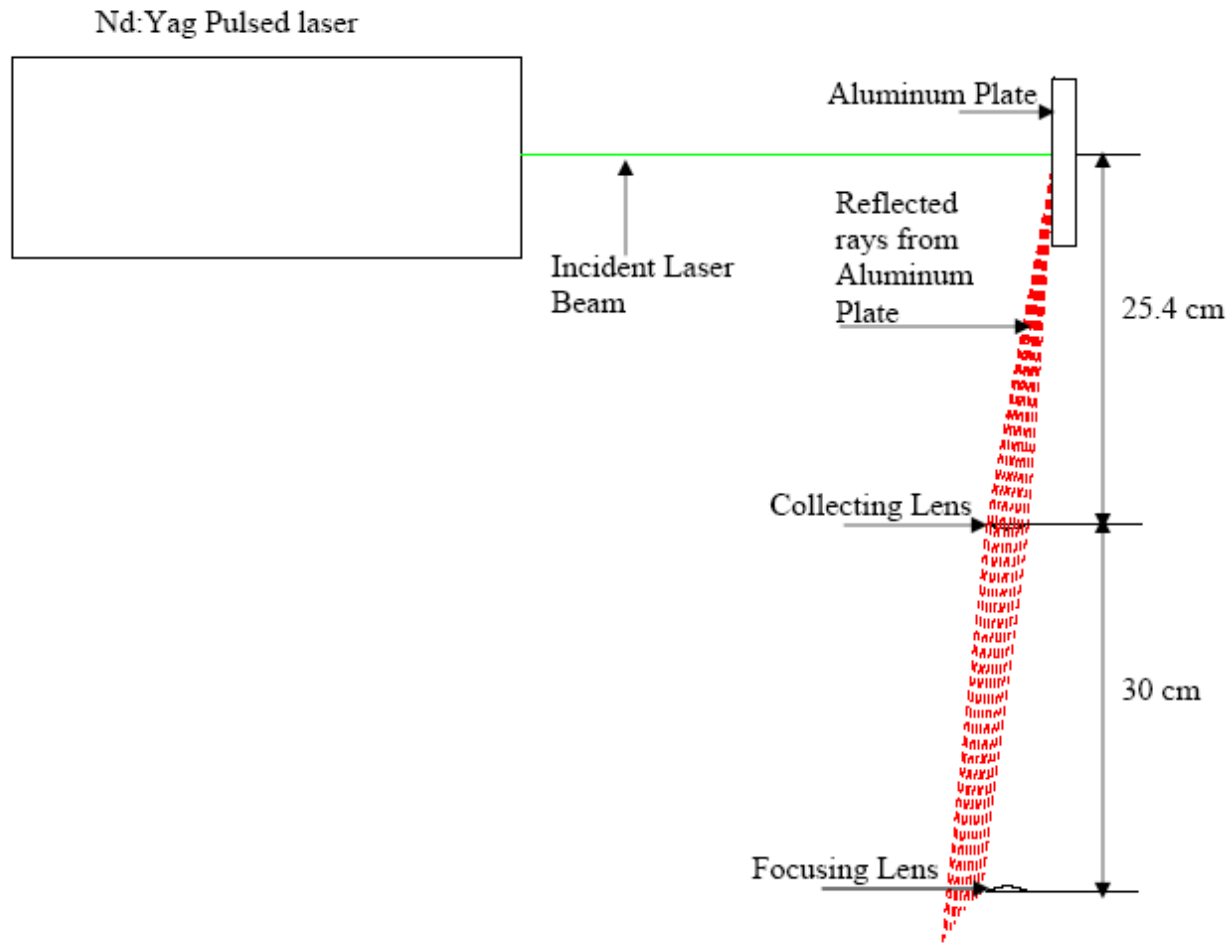


Figure 4-9. Ray tracing output from MATLAB when the aluminum plate is 7 cm from the nozzle.

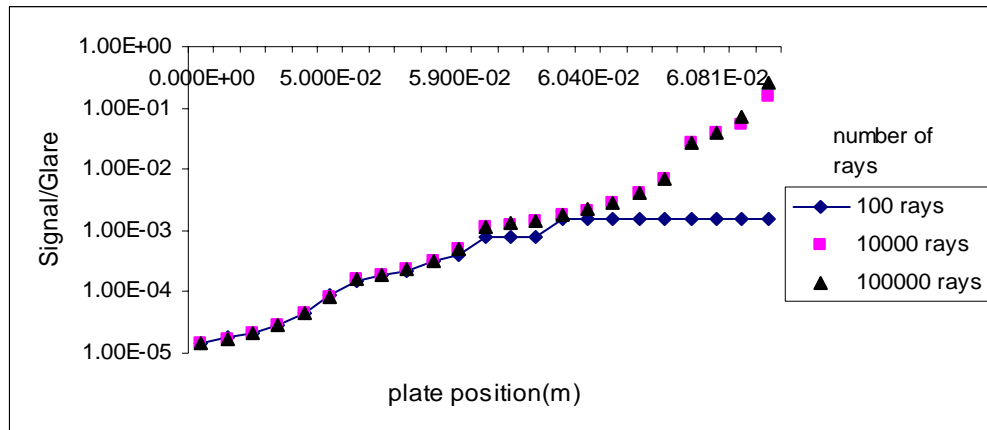


Figure 4-10. Glare for different plate positions as a function of number of rays.

It was observed that when 100 rays were used the glare initially decreased as the plate was moved away from the nozzle and then the glare became constant at a plate position of 0.0603 m from the control volume. When 10000 rays were used the accuracy of the code increased and the glare decreased as expected when the plate was moved away from the nozzle and was not constant as was the case when 100 rays were used. When 100000 rays are used the accuracy of the code further increased and the glare decreased as the plate was moved away from the control volume.

Figure 4-11 shows the glare from the aluminum plate as a function of plate position (for 532 nm, 355 nm and 1064 nm). It was observed that the glare decreased as the plate was moved away from the nozzle as expected and there was exponential decrease in glare starting from a plate position of 6.08 cm from the nozzle and reached almost zero when the plate was at 6.083 cm from the nozzle.

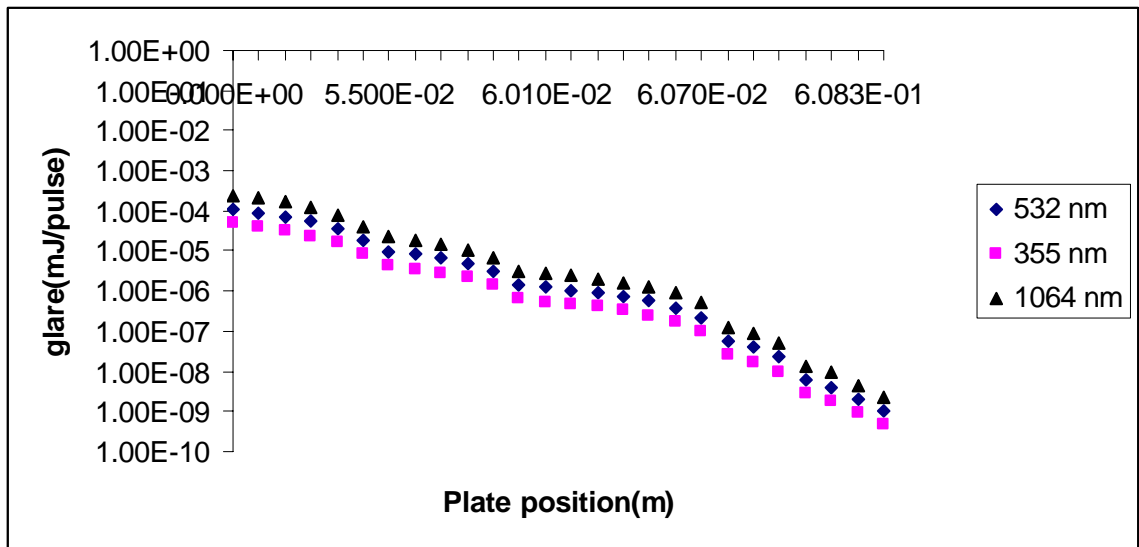


Figure 4-11. Glare as a function of plate position and wavelength. 100000 rays are used for the computation of the glare.

Experimental Methods

To measure the intensity of the scattered beam two different approaches are adopted. The first method involved calculating the integrated area under the voltage time curve and the second method involved using the peak. We conducted these studies to establish the use of peak voltage as a repeatable and reliable method of acquiring data rather than integrated area.

Integrated Area Method

This method involved calculating the full width half maximum area under the voltage time curve measured as the area between two points where the voltage is 50% of the maximum voltage. Initially 1000 data points per pulse are captured from the oscilloscope. A typical waveform captured from the oscilloscope is shown in Figure 4-12.

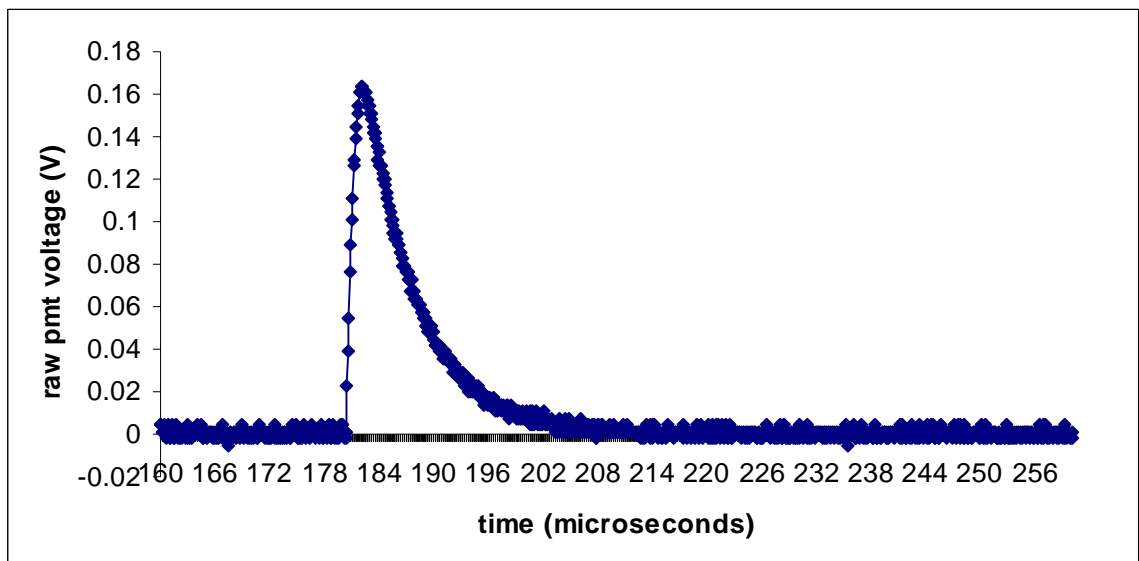


Figure 4-12. Typical waveform from a photomultiplier tube as captured by the oscilloscope. (Down stream distance of 4 nozzle diameters; $Re=100$; 100% Helium)

The full width half maximum area was calculated from the voltage time curve using the trapezoidal rule given by Equations 4-9 and 4-10.

$$A_i = \left(\frac{V_i + V_{i+1}}{2} \right) \Delta t \quad (4-9)$$

$$A = \sum_{i=1}^{1000} A_i \quad (4-10)$$

These measurements were done at a Reynolds number of 100 and at 4 nozzle diameters downstream with 100% helium flowing through the nozzle. These were done in the shear layer of the leak at a radial position of the nozzle corresponding to 60% helium. This is because it is at the shear layer; the maximum variation in the voltage was expected because jet fluctuations are greater there. The same procedure was repeated until the areas converged. Figure 4-13 shows the convergence studies for the full width half maximum area for both 355 nm and 532 nm wavelengths.

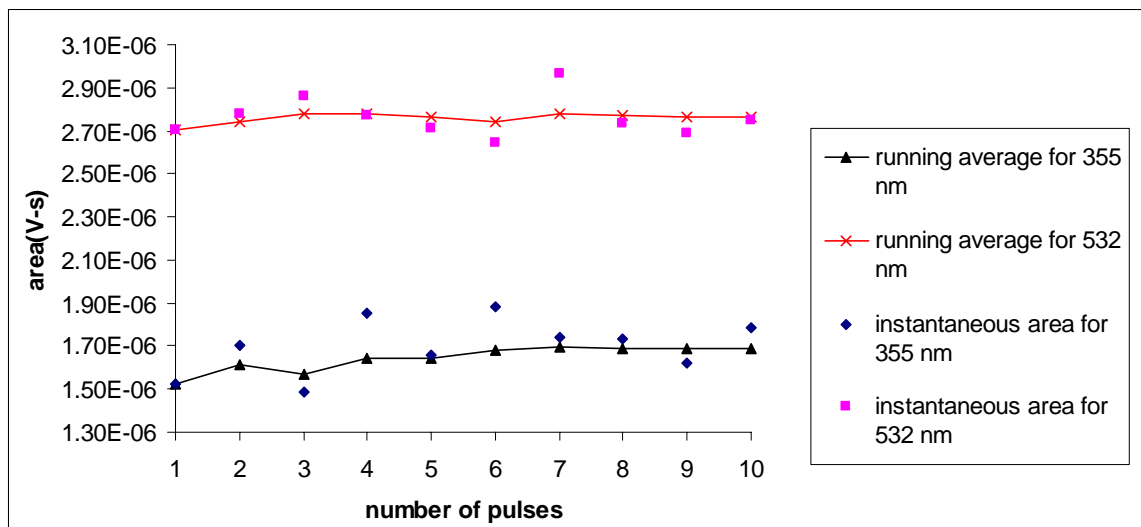


Figure 4-13. Running average of area for 355 and 532 nm

It was observed that the area converged after 10 pulses. Figure 4-14 shows the percent variation of the instantaneous area from the average area. Average area is the average of the areas of the 10 pulses and is calculated as given by Equation 4-11. It was observed that the percent variation was a maximum of 3.5%.

$$A_{avg} = \frac{\sum_{i=1}^{10} A_i}{10} \quad (4-11)$$

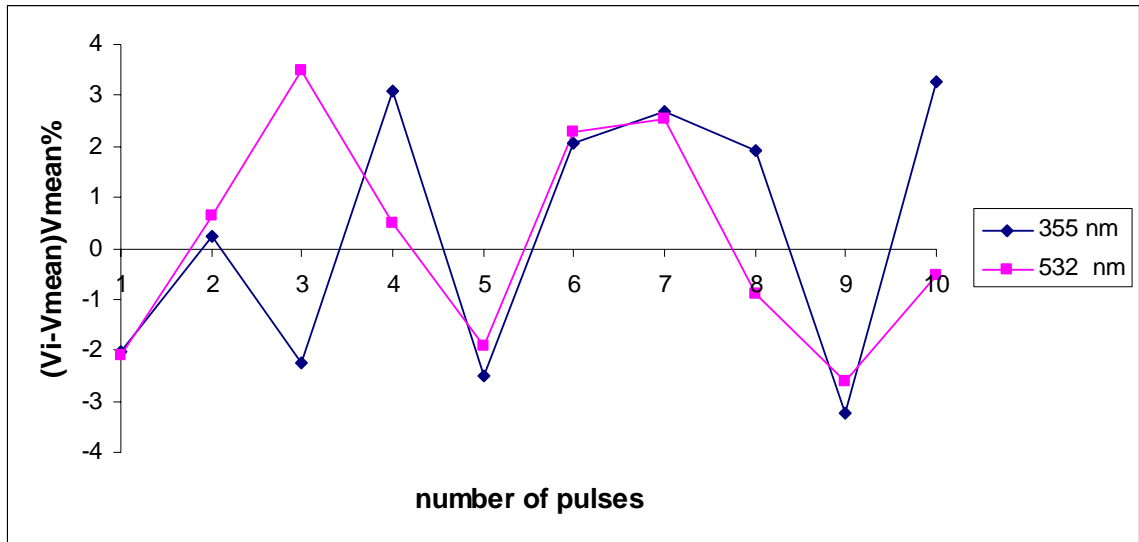


Figure 4-14. Percent variation in area for 355 nm and 532 nm

Peak Voltage Method

To establish the convergence of the peak voltage and the repeatability, two methods were adopted. First method involved recording the peak voltage from the voltage time curve from which the full width half maximum area is calculated (Figure 4-12 and Figure 4-13). Figure 4-15 shows the convergence studies for the peak voltage.

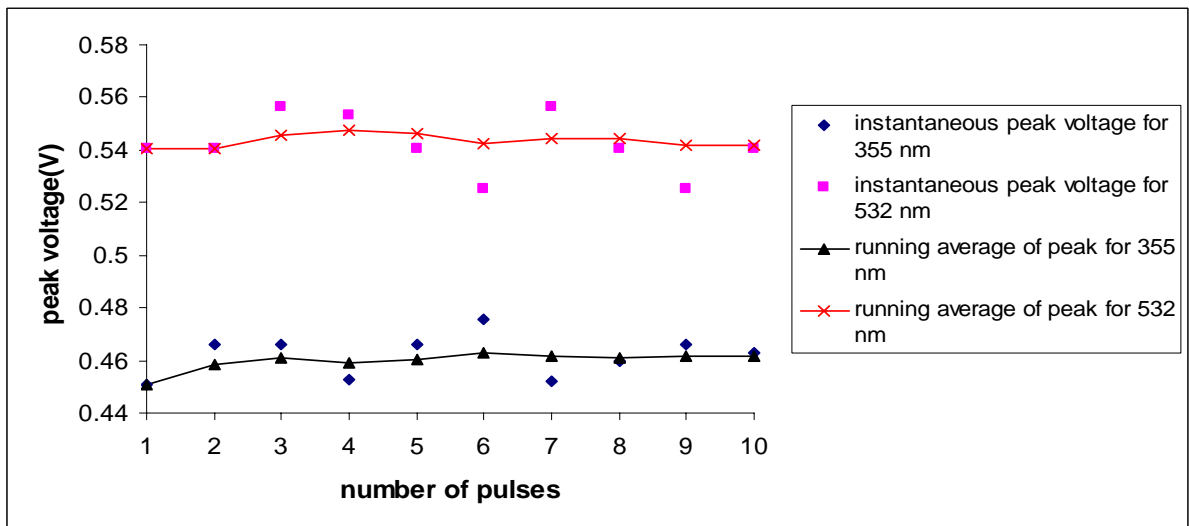


Figure 4-15. Running average of peak voltage for 355 nm and 532 nm

It was observed that the peak voltage converged after 10 pulses and the percent variation between the instantaneous peak and the average peak was 3% (Figure 4-16).

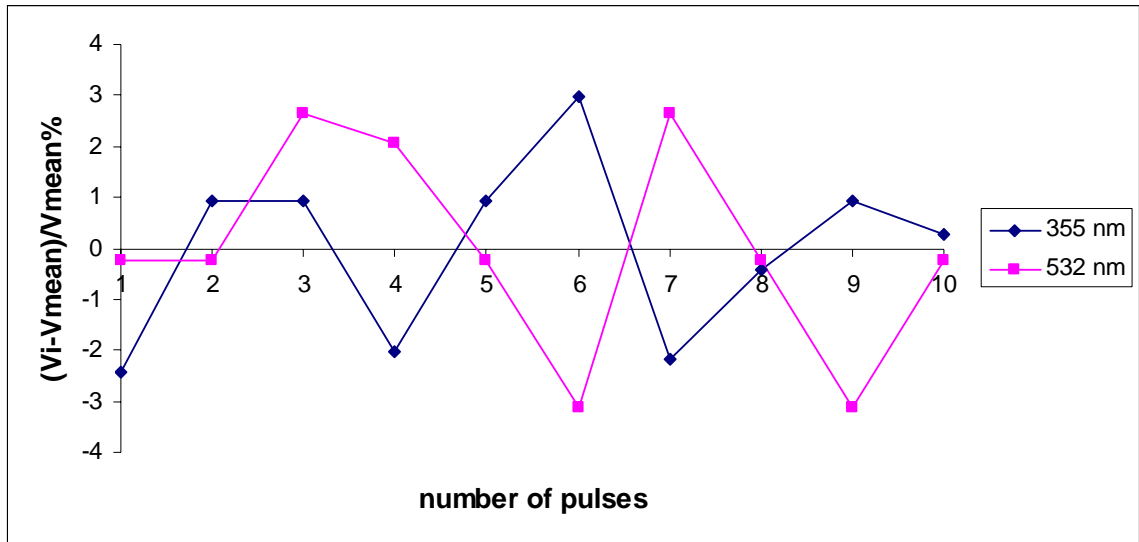


Figure 4-16. Percent variation in peak voltage for 355 nm and 532 nm

The second method involved recording the average peak voltage from the oscilloscope after 0, 100, 200, 300, 400 and 500 pulses and the percent variation in the average peak was calculated. Table 4-1 shows the voltage recorded for each measurement and also the percent variation between in the peak voltage after 100, 200, 300, 400 and 500 pulses.

It was observed that the percent variation in the average peak was less than 1% after 300 pulses. All these measurements were taken when 100% helium was flowing through the nozzle and in the shear layer at a radial position of the nozzle where the helium concentration was 60%

Table 4-1. Percent variation in average peak voltage for 355 nm and 532 nm

Pulse Number	Peak voltage 355 nm	Peak voltage 532 nm	% variation in peak voltage between two measurements for 355 nm	% variation in peak voltage between two measurements for 532 nm
1	460	552		
100	443	533	3.837	3.564
200	447	525	0.894	1.523
300	444	526	0.675	0.190
400	441	529	0.680	0.567
500	443	531	0.451	0.376

Peak Area Correlation

A correlation study was done between peak and integrated area and it was observed that the correlation coefficient between peak and area was 99.1% for both 355 nm and 532 nm (Figure 4-17).

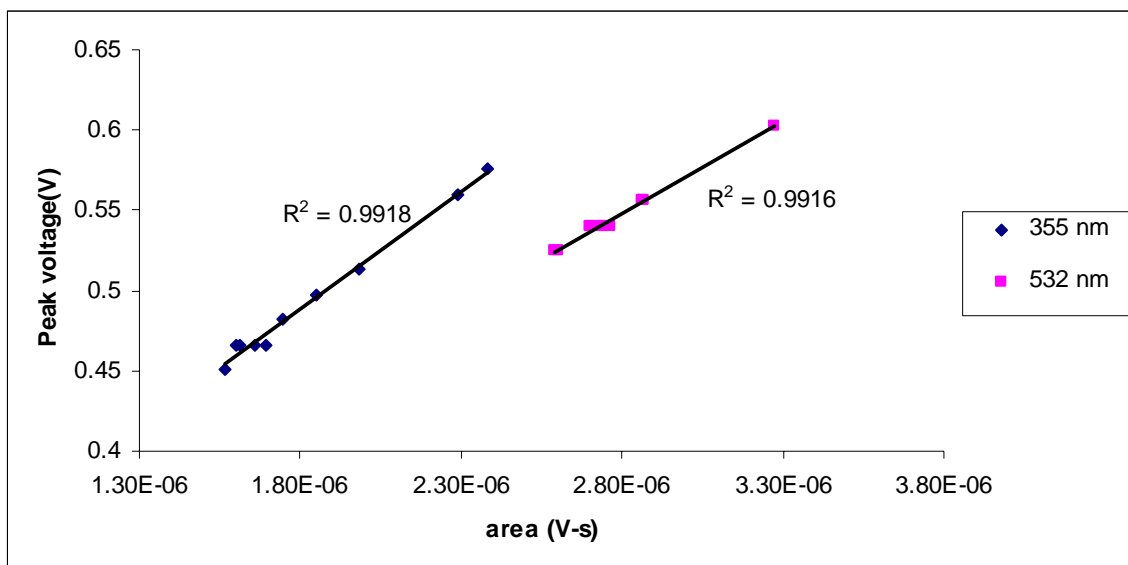


Figure 4-17. Correlation between peak voltage and area for 355 nm and 532 nm

So it was established that recording the average peak voltage after 300 pulses is a reliable way of recording data and provides all the important information that is needed to analyze the readings.

CHAPTER 5
RESULTS AND DISCUSSION

Numerical Results

As mentioned in chapter 4, a numerical code in MATLAB was written to compute the glare numerically. The glare was computed as a function of plate position for the two different wavelengths.

Figure 5-1 shows the Signal to glare ratio for different wavelengths as a function of plate position. To compute the signal-to-glare ratio, first the theoretical Rayleigh signal was calculated as given by the Equation 3-3 in chapter 3. Then the Rayleigh light scattering signal was divided by the glare which was computed numerically as discussed in chapter 4. As expected the Signal-to-glare ratio increased as the wavelength decreased because of the inverse fourth power dependence of Rayleigh signal on wavelength and also the Signal-to-glare ratio increased as the aluminum plate was moved away from the control volume.

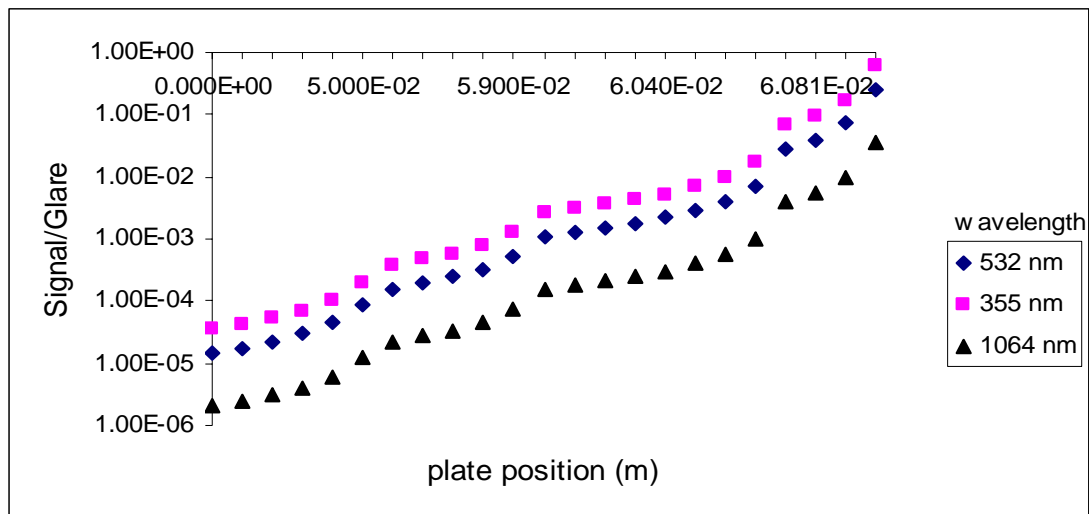


Figure 5-1. Signal to glare ratio as a function of plate position.

To compare the experimental and theoretical results, the normalized voltage was calculated for each case. This was done because the numerical code computes the glare from the aluminum plate alone and does not take into account the glare from the background surfaces, whereas the experimental results incorporated the glare from the aluminum plate and also the glare from the background surfaces. To account for this, the photomultiplier-tube voltage was normalized with respect to the maximum and minimum voltage as given by the Equation 5-1. The percent error in the theoretical and experimental results is a maximum of 5%.

$$\text{Voltage ratio} = \frac{V_i - V_{\min}}{V_{\max} - V_{\min}} \quad (5-1)$$

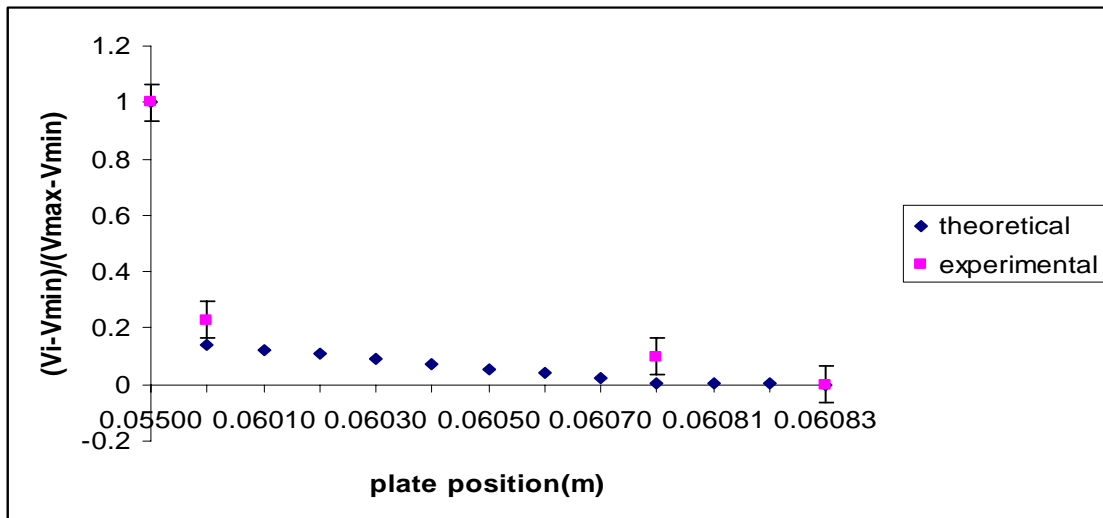


Figure 5-2. Comparison of experimental and theoretical glare as a function of plate position.

Experimental Results

Testing the Linearity of the Photomultiplier-tube Output Voltage

This section discusses how the output voltage from the photomultiplier-tube was tested to make sure that it was in the linear range. The laser power was varied from 0.9 kV to 1.31 kV and a power meter was used to monitor the incident laser power. As the

laser power was varied, the corresponding photomultiplier-tube voltage and the photodiode voltage were recorded. Figure 5-3 shows the variation of the photomultiplier and the photodiode voltages as a function of the power meter voltage. These readings were taken at 4 nozzle diameters downstream and without any gas flowing through the nozzle. The voltages recorded from the photomultiplier-tube, photodiode and the power meter were normalized according to Equation 5-1. It was observed that the voltages of both the photomultiplier and the photodiode increased linearly as the power meter voltage increased.

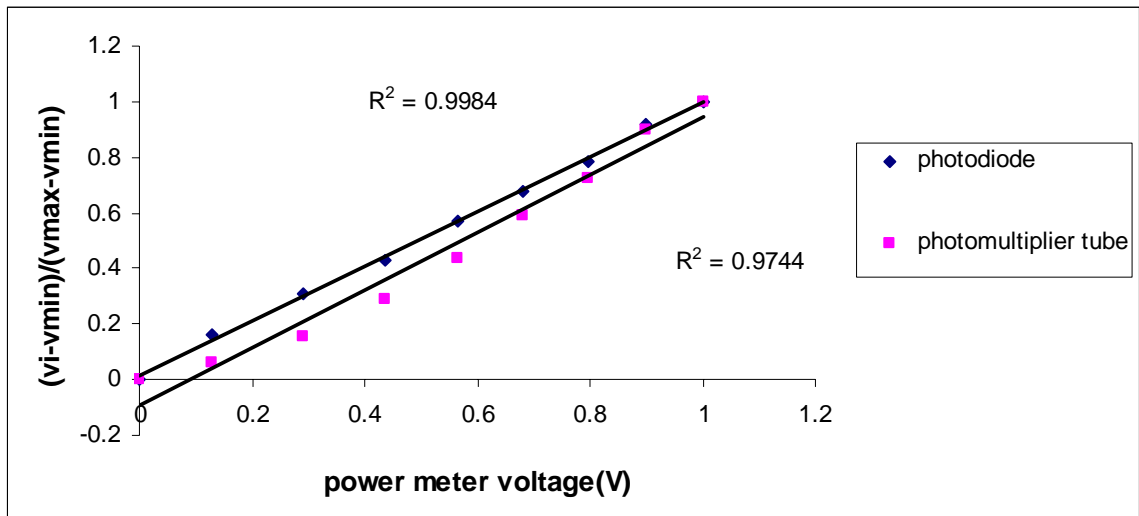


Figure 5-3. Photomultiplier tube and the photodiode voltage as a function of the power meter voltage.

The photomultiplier tube had a correlation coefficient, R^2 value of 0.9744 and the photodiode had a R^2 value of 0.9984.

The next study done was to ensure the linearity of the output voltage from the photomultiplier tube when the glare was varied in the presence of the aluminum plate. To do this the laser power was varied from 0.9 kV to 1.31 kV. The glare was varied by placing the aluminum plate in two positions directly in line with the incident laser beam. The incident laser power was monitored with a power meter when there was no plate.

These measurements were done at a nozzle position of 4 nozzle diameters downstream and with no gas flowing through the nozzle. The photomultiplier tube voltages are normalized using Equation 5-1. Figure 5-4 shows the variation of the photomultiplier tube voltage as a function of the power meter voltage.

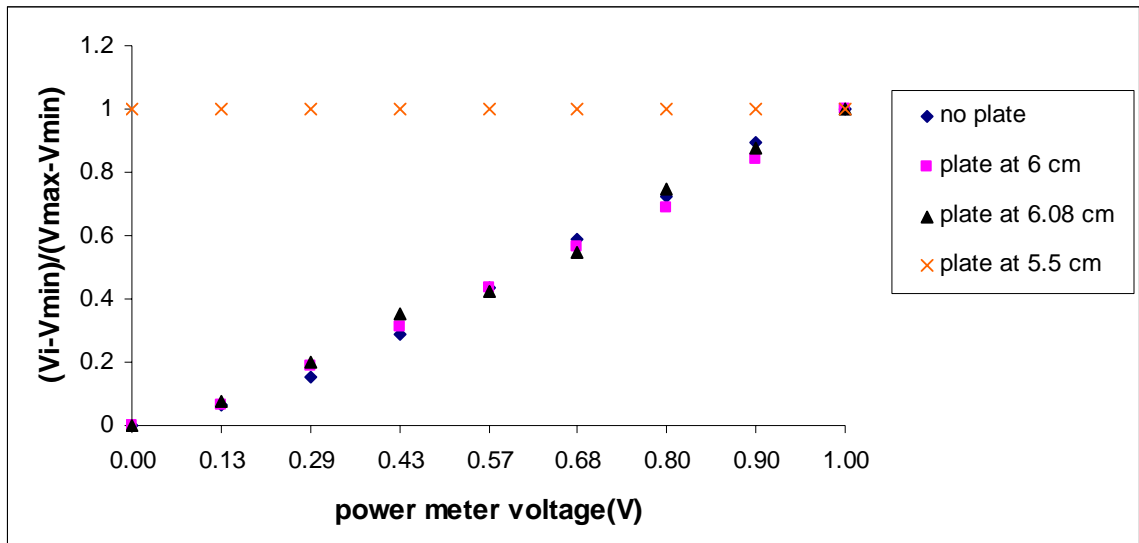


Figure 5-4. Photomultiplier tube voltage as a function of the power meter voltage when the glare is varied using an aluminum plate.

It was observed that the photomultiplier tube voltage increased linearly as the power meter voltage increased even in the presence of the aluminum plate. The correlation coefficient value, R^2 when there was no plate is 0.9744 and the value of R^2 when the plate was at 6.08 cm from the nozzle is 0.9922 and the R^2 value when the plate was at 6 cm from the nozzle is 0.9939. When the aluminum plate was placed at a distance of 5.5 cm from the nozzle, the glare was too high and there was no change in the photomultiplier tube voltage. To test the linearity of the photomultiplier tube voltage when the aluminum plate was placed at a distance of 5.5 cm from the nozzle, neutral density filter was used. The main purpose of using a neutral density filter is to reduce the amount of light that can pass through a filter. Neutral density filters absorb or reflect

fraction of light incident upon them. Neutral density filters are usually rated in optical density numbers. Optical density is the degree of opacity of a translucent medium. It is given by the Equation 5-2, where T is the transmission of the filter.

$$O.D = -\log_{10} T , \quad (5-2)$$

Table 5-1. Optical density and the corresponding transmission of neutral density filters. (Source: <http://www.evetar.com/product/6.asp>, Last accessed December 6th, 2004).

Optical Density	Transmission
0.1	80%
0.2	63%
0.3	50%
0.4	40%
0.5	32%
0.6	25%
0.7	20%
0.8	16%
0.9	13%
1.0	10%

To check the linearity of the photomultiplier tube voltage, the photomultiplier-tube voltage was recorded when the aluminum plate was at 5.5 cm from the nozzle and with no neutral density filter. Then a 0.6 density filter was used and the voltage from the photomultiplier tube was recorded and the procedure was repeated as the laser power was varied. It was observed that the voltage from the photomultiplier tube decreased to 25% as compared to the voltage when there was no neutral density filter. Since the transmission of a 0.6 density filter was 25%, it was established that the photomultiplier tube is operating in the linear range.

Table 5-2. Photomultiplier-tube voltages before and after using the 0.6 neutral density filter.

Laser Power	Photomultiplier-tube voltage before using neutral density filter for 532 nm	Photomultiplier-tube voltage before using neutral density filter for 355 nm	Photomultiplier-tube voltage with neutral density filter for 532 nm (% decrease)	Photomultiplier-tube voltage with neutral density filter for 355 nm (% decrease)
0.9	1.562	1.012	0.389 (25.1%)	0.251 (24.8%)
1	1.562	1.325	0.390 (25%)	0.330 (24.9%)

Eliminating Glare from the Rayleigh Light Scattering Signal

This section discusses how the glare was eliminated from the Rayleigh light scattering signal. To eliminate the glare from the Rayleigh signal, two approaches were adopted.

Reference value method

This method involved recording the photomultiplier-tube voltage when there was no gas flowing through the nozzle for every radial position of the nozzle and for every plate position. The voltage recorded by the photomultiplier-tube was due to glare from the background surfaces, Mie scattering and scattering due to air molecules. It is written mathematically as

$$V_{ref} = V_{Glare} + V_{Mie\ Scattering} + V_{air} \quad (5-3)$$

Next, the photomultiplier tube voltage was recorded when a mixture of 80% nitrogen and 20% helium was flowing through the nozzle. The diameter of the laser at the control volume was 8mm and the distance between the edges of the shear layers of the jet was 5.8mm. Hence there was entrainment of air in the control volume. Hence the voltage recorded by the photomultiplier-tube was because of the glare from the

background surfaces, Mie scattering, and scattering due to the mixture of helium and nitrogen molecules (leaking fluid) and scattering due to air molecules. It is written mathematically as, where x is the percentage of the leaking fluid present in the control volume.

$$V_{act} = V_{Glare} + (V_{Mie\ Scattering} + V_{air})(1 - x) + V_{leak}x \quad (5-4)$$

When the two equations are subtracted, glare and the Mie scattering was eliminated from the Rayleigh signal. It is written mathematically as

$$V_{RLS} = x(V_{leak} - V_{air} - V_{Mie\ Scattering}) \quad (5-5)$$

Hence the glare was eliminated from the Rayleigh light scattering signal. But as there was entrainment of air in the control volume (Equation 5-5) the signal is always higher than the predicted signal (theoretically) as the scattering cross-section of air 1.32 times that of nitrogen and the entrained aerosols will scatter in the Mie regime.

Assuming that the ratio of the glare at the two wavelengths is constant

As discussed in chapter 3, an aluminum plate was used to vary the glare. This method takes into consideration that the irradiance from the aluminum plate was much higher as compared to the irradiance from other surfaces.

From Equation 3-18, the scattering intensity is written as

$$I_{Scat} = I_{RLS} + I_{Glare} \quad (3-18)$$

From Equation 3-17, the Rayleigh light signal is proportional to the scattering cross-section of the gas and the incident intensity of the laser. Hence the ratio of the Rayleigh light signal at the two wavelengths is the ratio of the scattering cross-sections.

$$\frac{I_{RLS,\lambda 1}}{I_{RLS,\lambda 2}} = \frac{\sigma_{\lambda 1} I_{o,\lambda 1}}{\sigma_{\lambda 2} I_{o,\lambda 2}} = S \left(\frac{I_{o,\lambda 1}}{I_{o,\lambda 2}} \right) \quad (5.6)$$

The intensity of the glare I_{Glare} is written as $\sum_{i=1}^n G_i A_i$ where A_i is the area of the background surface visible to the detector and G_i is the irradiance from i^{th} surface. The irradiance from the surface is proportional to the reflectivity of the surface. As the area of the surface visible to the two detectors is same, the ratio of the glare at two wavelengths was the ratio of the reflectivity of the surface at those two wavelengths. Since different surfaces have different reflectivities, the ratio of the glare is not constant. We used an aluminum plate to vary the glare. It was proved that the irradiation from the aluminum plate was much more compared to the irradiation from other surfaces.

$$\sum G_{pl} A_{pl} \gg \sum_{i=2}^n G_i A_i \quad (5-7)$$

The ratio of the glare in this case was just the ratio of the reflectivity of the aluminum plate. Since the ratio of the reflectivity of the aluminum plate was constant, the ratio of the glare was constant and is written as

$$\frac{I_{Glare,\lambda 1}}{I_{Glare,\lambda 2}} = \frac{\rho_{\lambda 1} I_{o,\lambda 1}}{\rho_{\lambda 2} I_{o,\lambda 2}} = R \left(\frac{I_{o,\lambda 1}}{I_{o,\lambda 2}} \right) \quad (5-8)$$

As discussed in chapter 4, the intensity of the light incident at the photomultiplier-tube at the two wavelengths is given by the Equations 5-9 and 5-10.

$$I_{Scat,\lambda 1} = I_{RLS,\lambda 1} + I_{Glare,\lambda 1} \quad (5-9)$$

$$I_{Scat,\lambda 2} = I_{RLS,\lambda 2} + I_{Glare,\lambda 2} \quad (5-10)$$

From Equation 5-6 the ratio of the Rayleigh light scattering signal at the two wavelengths is S and from Equation 5-8, the ratio of the glare at the two wavelengths is R. Solving Equations 5-6, 5-8, 5-9 and 5-10 simultaneously, the Rayleigh light signal at the two wavelengths was written as

$$I_{RLS,\lambda 1} = \frac{S(I_{Scat,\lambda 1}I_{o,\lambda 2} - RI_{Scat,\lambda 2}I_{o,\lambda 1})}{(S - R)(I_{o,\lambda 2})} \quad (5-11)$$

And

$$I_{RLS,\lambda 2} = \left(\frac{I_{RLS,\lambda 1}}{S} \right) \left(\frac{I_{o,\lambda 2}}{I_{o,\lambda 1}} \right) \quad (5-12)$$

Equations 5-11 and 5-12 gave the Rayleigh light scattering signal with the glare decoupled from them.

Theoretical and Experimental Photon-arrival Rates

This section discusses how the theoretical and the experimental photon-arrival rates compare.

Theoretical photon-arrival rate

As discussed in Chapter 3, the theoretical photon-arrival rate was calculated according to the formula

$$R_p = I_o(\eta)(d\omega)(dV)([N(x\sigma_{He} + (1-x)\sigma_{N_2})]) \quad (5-13)$$

Where

$$I_o \quad 200 \text{ mJ/Pulse} = 5.34\text{E}17 \text{ photons/pulse for } 532 \text{ nm}$$

$$\text{And } 75 \text{ mJ/Pulse} = 2.00\text{e}17 \text{ photons/pulse for } 355 \text{ nm}$$

$$\eta \quad 0.59049.$$

$$dV \quad 0.118 \text{ mm}^3.$$

$$d\omega \quad \frac{\pi(60)^2}{(250)^2}.$$

$$N \quad 2.25\text{E}25 \text{ molecules/m}^3$$

$$x \quad \text{percentage of helium.}$$

Table 5-3. Scattering cross-sections (of helium, nitrogen, hydrogen and air) at 532 nm and 355 nm.

Gas	Scattering cross-section at 532 nm, $\sigma_{\lambda 1}$	Scattering cross-section at 355 nm, $\sigma_{\lambda 2}$
Helium	1.22E-33	6.17E-33
Nitrogen	6.15E-32	3.10E-31
Hydrogen	1.89E-32	9.53E-32
Air	8.16E-32	4.11E-31

The percentage of helium was decreased from 100 to 0 and the percentage of nitrogen was increased from 0 to 100 and the resulting photon-arrival rate for both 355 nm and 532 nm is shown in Figure 5-5.

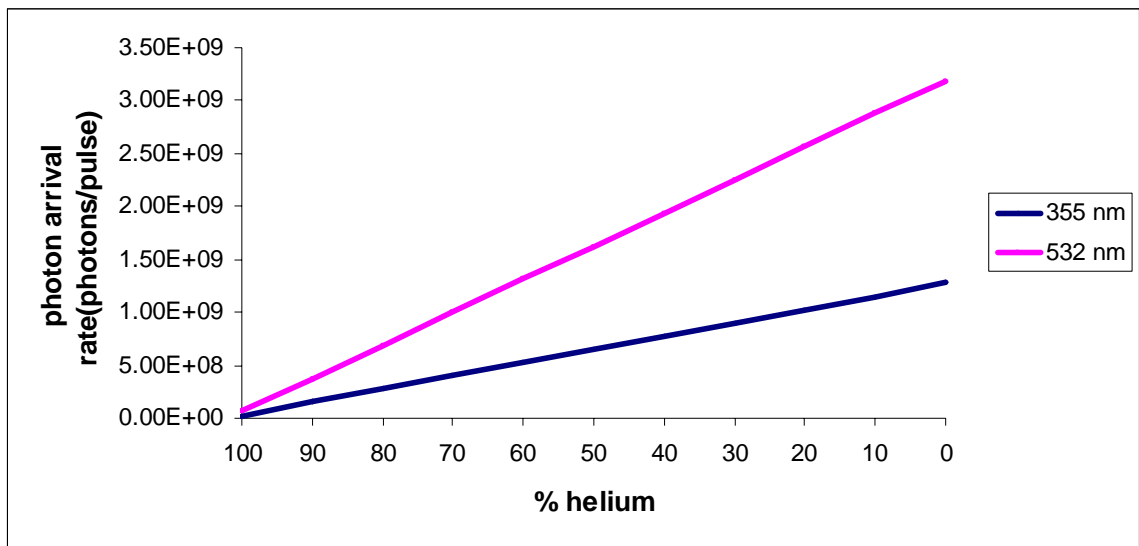


Figure 5.5 Theoretical photon-arrival rates for 355 nm and 532 nm.

Experimental photon-arrival rate

To calculate the experimental photon-arrival rates, a mixture of helium and nitrogen was used and the measurements were done at a nozzle position of 4 nozzle diameters downstream and the Reynolds number used was 100. The percentage of Helium was decreased from 100 to 0 and the percentage of nitrogen was increased from 0

to 100 and the corresponding waveforms of the photomultiplier-tube are recorded from the oscilloscope. The area under the voltage time curve was calculated as discussed in chapter 4 using the Equations 4-9 and 4-10. Then the area which has units of volts-sec was converted to photons per pulse using the Equation 5-14, where C_{PMT} is the photomultiplier tube calibration constant and is obtained from the manufacturers specifications. It has a value of 121 V/nW for 532 nm and 244 V/nW for 355 nm.

$$R_{p,Experimental} = \frac{A_{PMT} \lambda}{C_{PMT} hc} \quad (5-14)$$

The glare from the experimental photon-arrival rate was reduced using the reference value method. Figure 5-6 shows the comparison of the experimental and the theoretical photon-arrival rates.

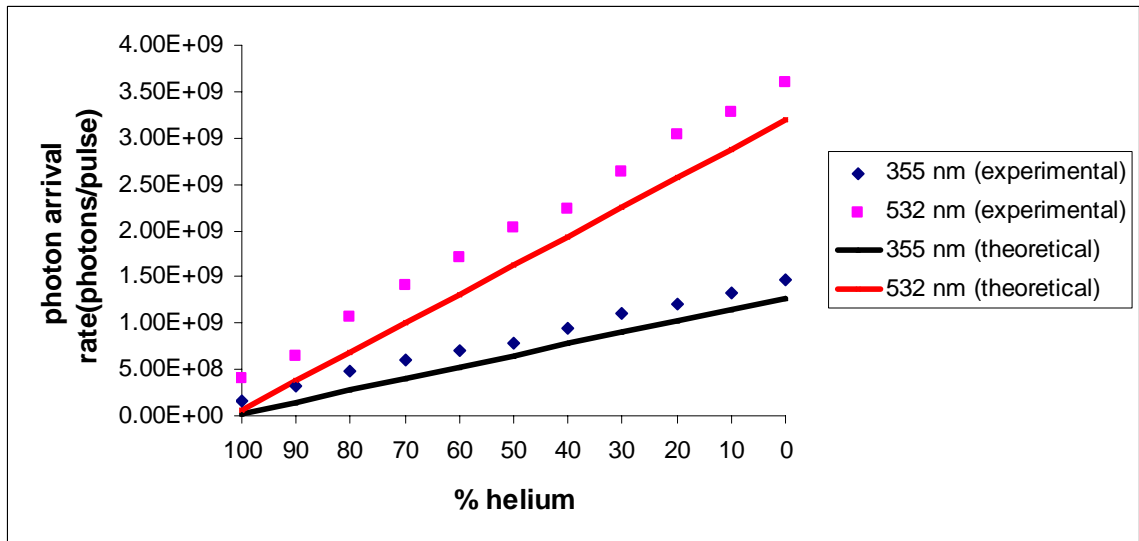


Figure 5-6. Comparisons of theoretical and experimental photon-arrival rates for 355 nm and 532 nm.

Figure 5-7 shows the percent error between experimental and theoretical photon-arrival rates for 532 nm and 355nm. The percentage uncertainty due to electronic shot noise was less than 0.1% for an averaging time of 0.001 sec. It is calculated according to the formula

$$\overline{\omega}_{R_p} = \frac{1}{\sqrt{R_p \Delta t}} \quad (5-15)$$

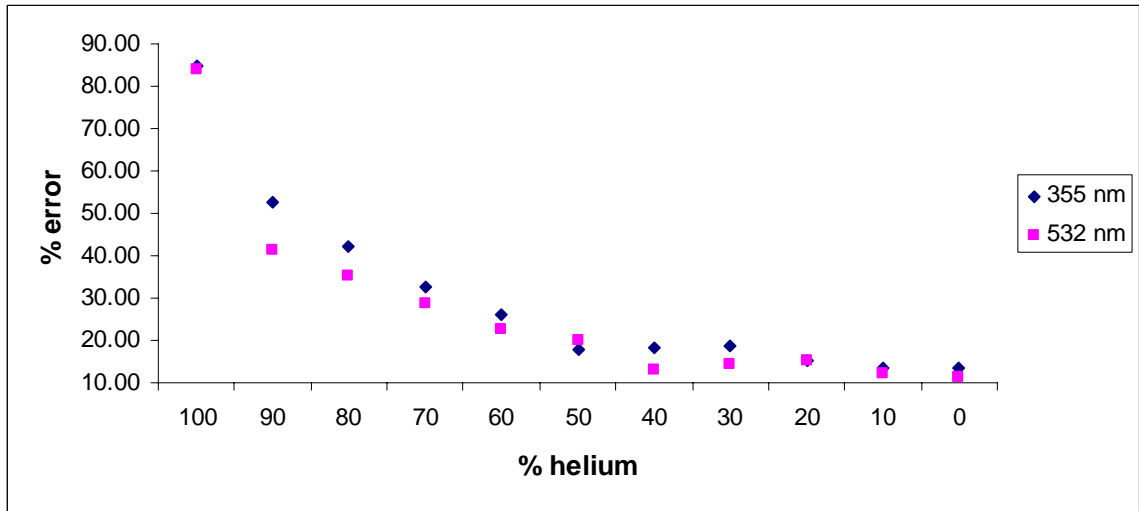


Figure 5-7. Percent error between theoretical and experimental photon-arrival rates as shown in Figure 5-6

It was observed that the maximum error is around 80% for 100% helium and the percentage error gradually decreased thereafter. This error is attributed to two facts.

- The diameter of the laser at the control volume was 8 mm and the distance between the edges of the shear layers of the jet was 5.8 mm. As a result of this there was entrainment of air in the control volume. As the scattering cross-section of air was more than helium and nitrogen, the intensity of the scattered beam as detected by the photomultiplier-tube was increased.
- The optical efficiency of the collection optics may deviate from the assumed 90%.

Analysis of the Recorded Data

Raw photomultiplier-tube voltage variation

This section discusses how the recorded data was analyzed to predict the presence of hydrogen in the jet and to eliminate the glare from the Rayleigh light signal. Figure 5-8 shows the variation of the raw peak voltage as a function of the radial position when there was no plate and when the plate was at 6.083 cm, 6.08 cm, 6 cm and 5.5 cm from the nozzle for 532 nm wavelengths. The peak voltage was converted into mJ/pulse using

the photomultiplier-tube calibration constant provided by the manufacturer. These measurements were taken at a downstream location of 4 nozzle diameters and when a mixture of 20% helium and 80% nitrogen was flowing through the nozzle. This mixture was used because the scattering cross-section of the mixture of 20% helium and 80% nitrogen is equal to that of hydrogen. The scattering cross-section of hydrogen was 0.23 that of air (Table 5-3). The Reynolds number was 100. The x-axis is the radial position of the nozzle normalized with the downstream distance.

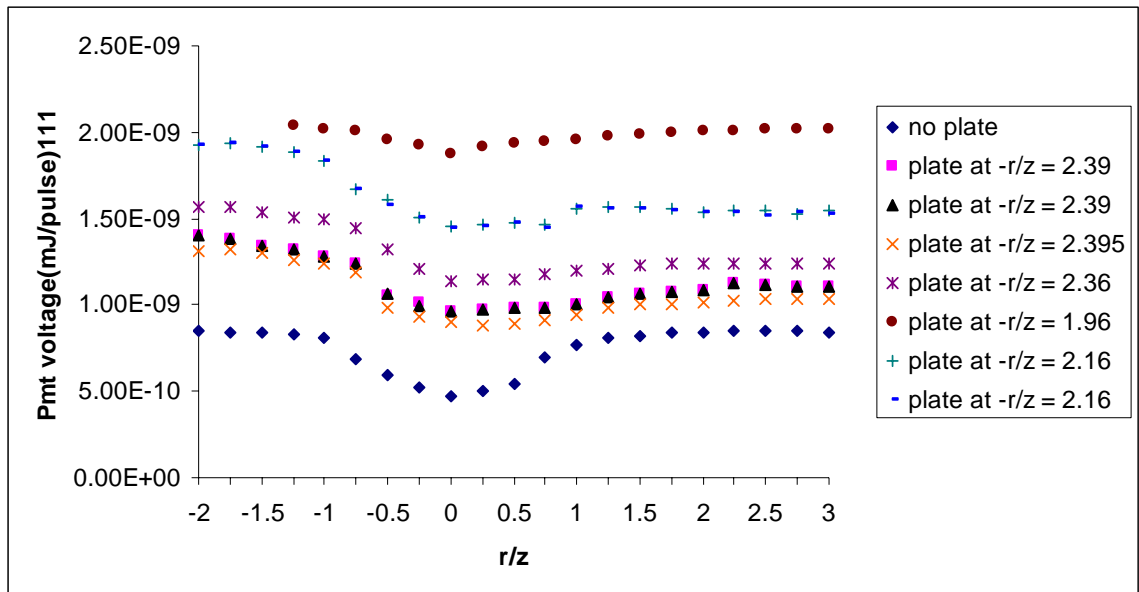


Figure 5-8. Raw photomultiplier-tube voltages as a function of radial and plate position for 532 nm. The measurements were taken at 4 nozzle diameters downstream for a mixture of 20% helium and 80% nitrogen

It was observed that the peak voltage was constant outside the shear layer as there was only ambient air outside the shear layer. The minimum peak voltage occurred at the jet centerline which corresponded to 100% hydrogen. The fall in voltage at the jet centerline occurred because the scattering cross-section of hydrogen was less than that of air and as discussed in chapter 3, the voltage output from the photomultiplier-tube is a function of the scattering cross-section of the gas. It was observed that the raw peak

voltage was not symmetric about the jet center line when the aluminum plate was used where as it was symmetric about the jet centerline when there was no plate. This is because when the plate was used, the glare was not constant and was higher when the nozzle was closer to the plate and gradually decreased as the nozzle was moved away from the plate. The glare from the aluminum plate was higher when the plate was at 5.5 cm and 5 cm from the nozzle and a neutral density filter of 0.6 optical density was used to attenuate the intensity of the scattered beam.

Figure 5-9 shows the variation of the raw peak voltage as a function of the radial position when there was no plate and when the plate was at 6.03 cm, 6.08 cm, 6 cm and 5.5 cm from the nozzle for 355 nm wavelengths. As observed from the Figure 5.8, there was a fall in voltage at the jet centerline corresponding to 100% hydrogen and the peak voltage was constant outside the shear layer.

As seen in Figures 5-8 and 5-9, two measurements were taken when the plate was at 6.08 cm and 5.5 cm from the nozzle. This was done to test the repeatability of the data.

Figure 5-10 shows the percentage error in the raw photomultiplier-tube voltages between the two measurements taken when the plate was at 6.08 cm and 5.5 cm from the nozzle for 532 nm and 355 nm. It was observed that the maximum error in the raw photomultiplier-tube voltage when the plate is at 6.08 cm from the nozzle is 5%. The maximum error when the plate was at 5.5 cm from the nozzle was 3%. Hence it was concluded that the data is repeatable and reproducible.

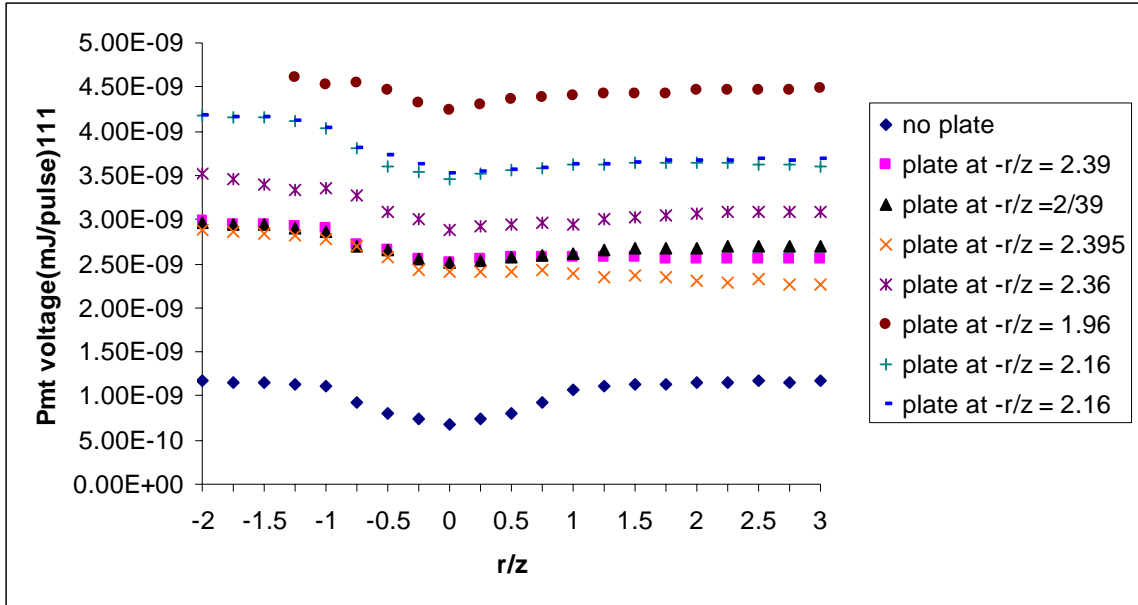


Figure 5-9. Raw photomultiplier-tube voltages as a function of radial and plate position for 355 nm. The measurements were taken at 4 nozzle diameters downstream for a mixture of 20% helium and 80% nitrogen

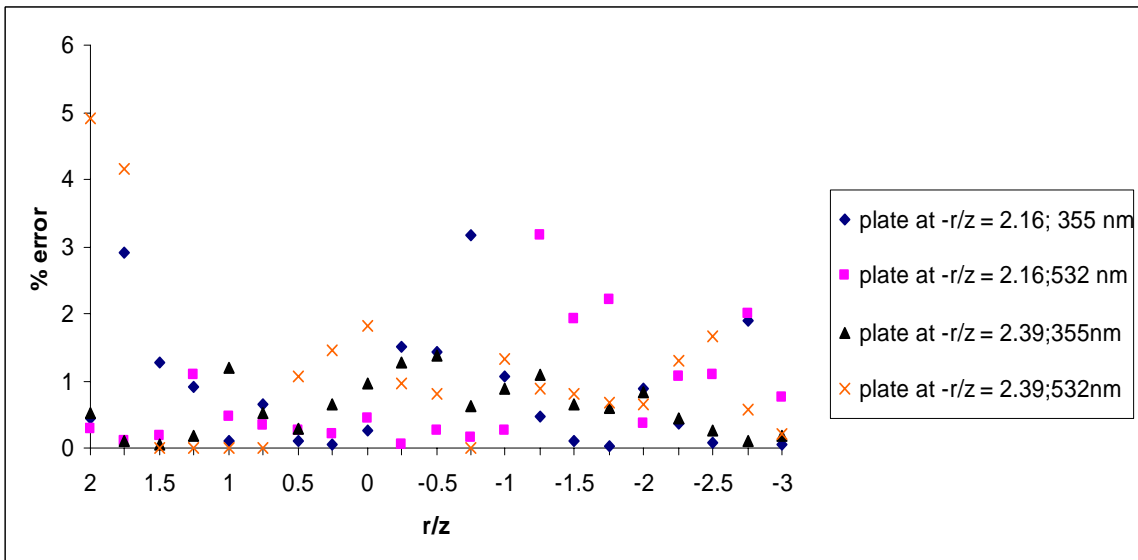


Figure 5-10. Percentage errors in raw photomultiplier-tube voltage for two typical plate positions as a function of radial position.

Variation of glare as a function of radial and plate position

Figure 5-11 shows the glare as a function of the radial position when there was no plate and when the plate was at 6.083 cm, 6.08 cm, 6 cm and 5.5 cm from the nozzle for 532 nm.

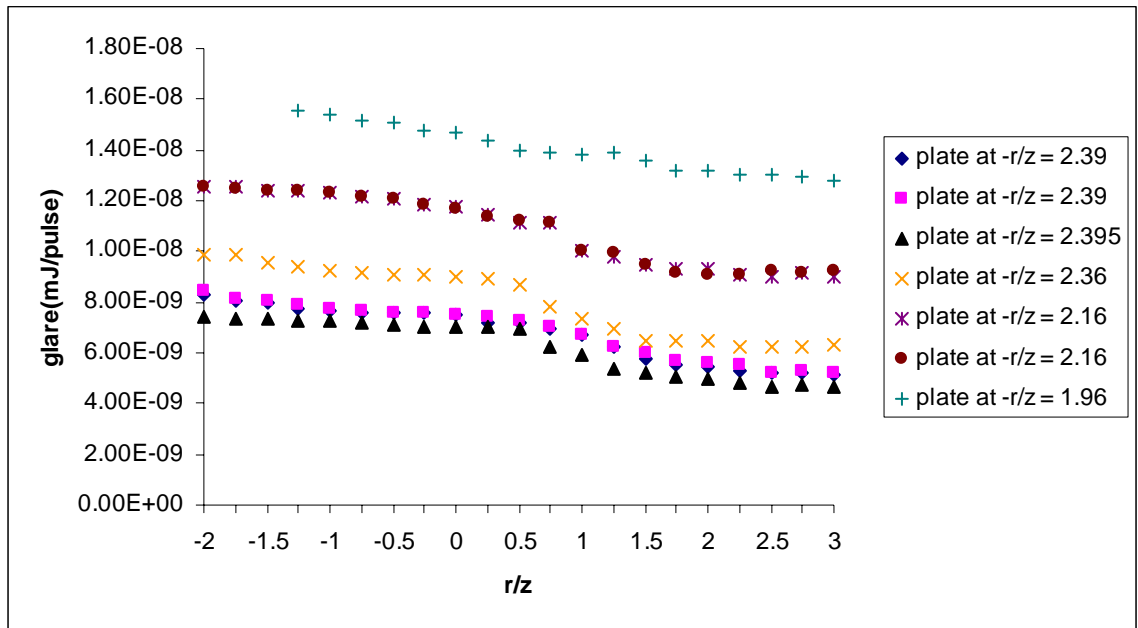


Figure 5-11. Glare as a function of radial and plate position for 532 nm for a downstream location of 4 nozzle diameters and when a mixture of 20% helium and 80% nitrogen is flowing through the nozzle.

It was observed that the glare was higher when the nozzle was closer to the plate and gradually decreased as the nozzle is moved away from the aluminum plate. The glare was calculated using the reference value method when there was no plate and when the plate was at 6.083 cm, 6.08 cm, 6 cm and 5.5 cm from the nozzle. When the plate was at 5.5 cm and 5 cm from the nozzle, the glare was calculated taking into consideration that the ratio of the glare at the two wavelengths was constant. The percentage error in the glare calculated by two methods for the case when the plate was at 5.5 cm from the nozzle was a maximum of 0.17%. So it was concluded that the two methods of calculating the glare agree well with each other.

Figure 5-12 shows the glare as a function of the radial position when there was no plate and when the plate was at 6.083 cm, 6.08 cm, 6 cm and 5.5 cm from the nozzle for 355 nm.

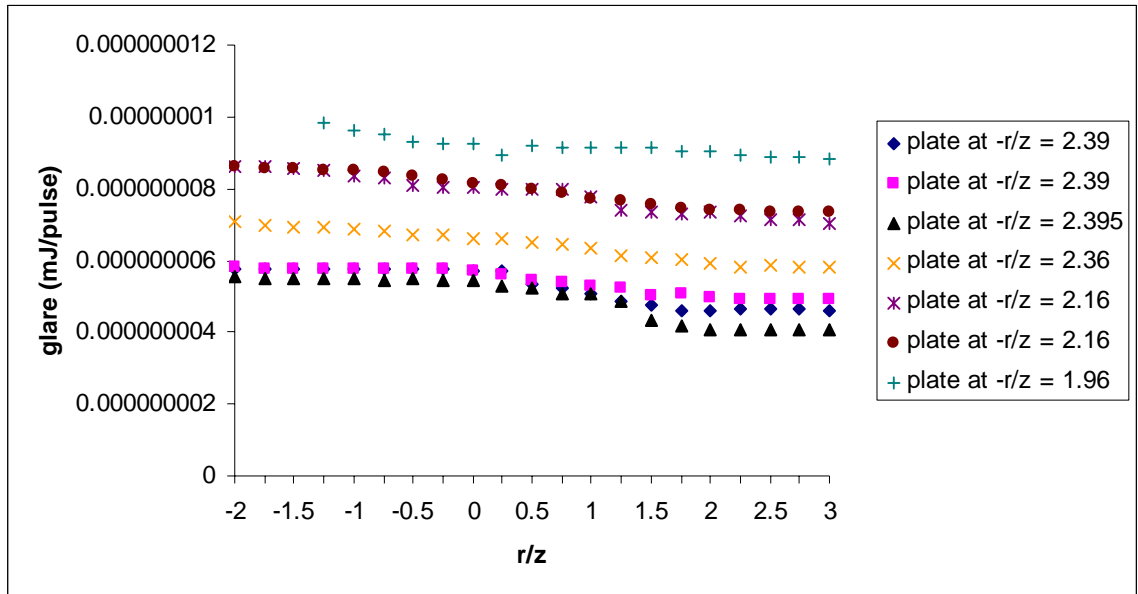


Figure 5-12. Glare as a function of radial and plate position for 355 nm for a downstream location of 4 nozzle diameters and when a mixture of 20% helium and 80% nitrogen is flowing through the nozzle.

As observed from Figure 5-11, it was observed that the glare was higher when the nozzle was closer to the plate and gradually decreased as the nozzle was moved away from the plate. The percentage error in the glare calculated by two methods for the case when the plate was at 5.5 cm from the nozzle was a maximum of 0.25%.

Variation of Rayleigh light scattering signal as a function of radial and plate position

Figure 5-13 shows the Rayleigh light scattering signal as a function of the radial position when there was no plate and when the plate was at 6.083 cm, 6.08 cm, 6 cm and 5.5 cm from the nozzle for 532 nm.

Reference value method was used to eliminate the glare from the raw peak voltage shown in Figure 5-8. It was observed that the Rayleigh light scattering signal is symmetric about the jet centerline as the glare was eliminated.

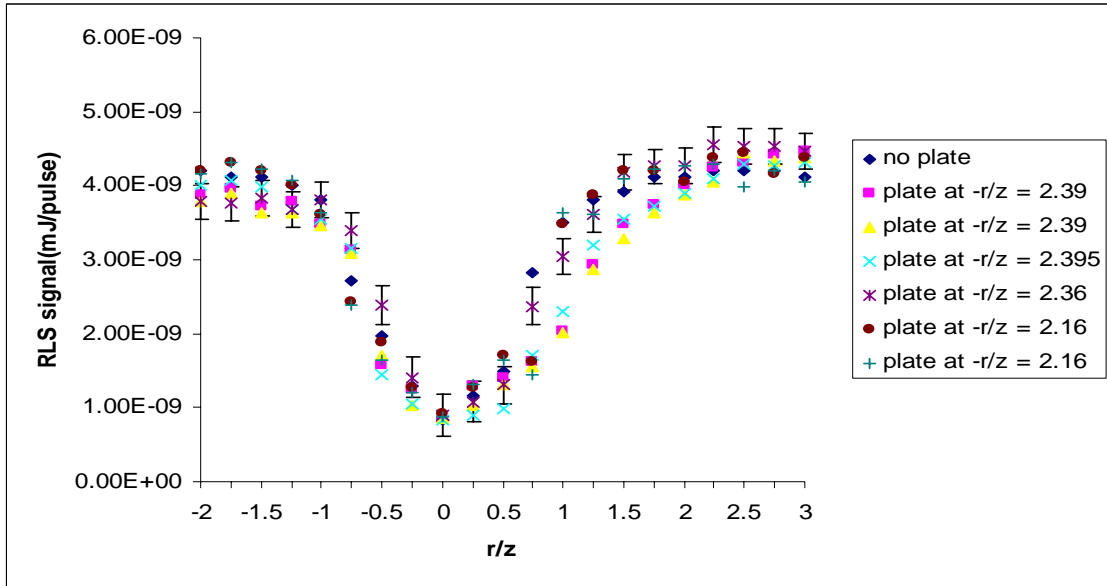


Figure 5-13. Rayleigh light scattering signal as a function of radial and plate position for 532 nm for a downstream location of 4 nozzle diameters and when a mixture of 20% helium and 80% nitrogen is flowing through the nozzle.

Error bars are shown for the case when the plate was at 6 cm from the nozzle. The error bars are calculated using the formula $\pm 3\delta$, where δ is the standard deviation in the Rayleigh light scattering signal. This is because 99.9% of the data points fall in the range of $\pm 3\delta$. The standard deviation was of the order of 0.1 for a signal of the order 1. The ratio of the maximum to the minimum voltage was around 5 and the fall in voltage was 20% which corresponded to the ratio of scattering cross-sections of air and hydrogen which was 4.31. The scattering cross-section of hydrogen and air are shown in Table 5-3.

Figure 5-14 shows the Rayleigh light scattering signal as a function of the radial position when there was no plate and when the plate was at 6.083 cm, 6.08 cm, 6 cm and 5.5 cm from the nozzle for 355 nm.

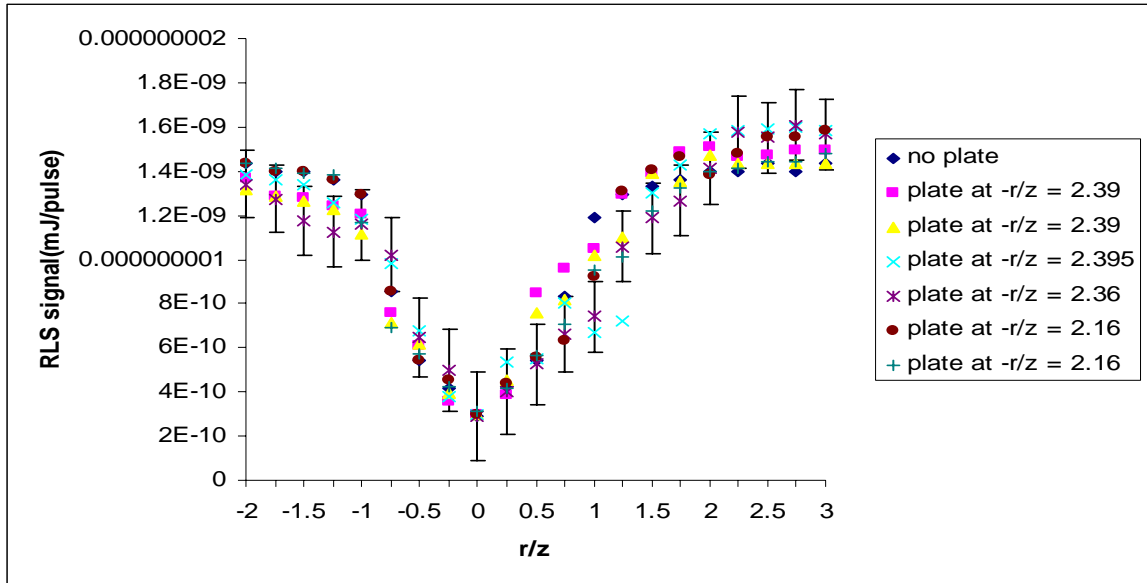


Figure 5-14. Rayleigh light scattering signal as a function of radial and plate position for 355 nm for a downstream location of 4 nozzle diameters and when a mixture of 20% helium and 80% nitrogen is flowing through the nozzle.

Reference value method was used to eliminate the glare from the raw peak voltage shown in Figure 5-9. It was observed that the Rayleigh light scattering signal was symmetric about the jet centerline as the glare was eliminated. Error bars are shown for the case when the plate was at 6 cm from the nozzle. The error bars are calculated according to the formula $\pm 3\delta$, where δ is the standard deviation of the Rayleigh light scattering signal.

Figure 5-15 shows the signal-to-glare ratio as a function of the radial position when there was no plate and when the plate was at 6.083 cm, 6.08 cm, 6 cm and 5.5 cm from the nozzle for 532 nm and 355 nm.

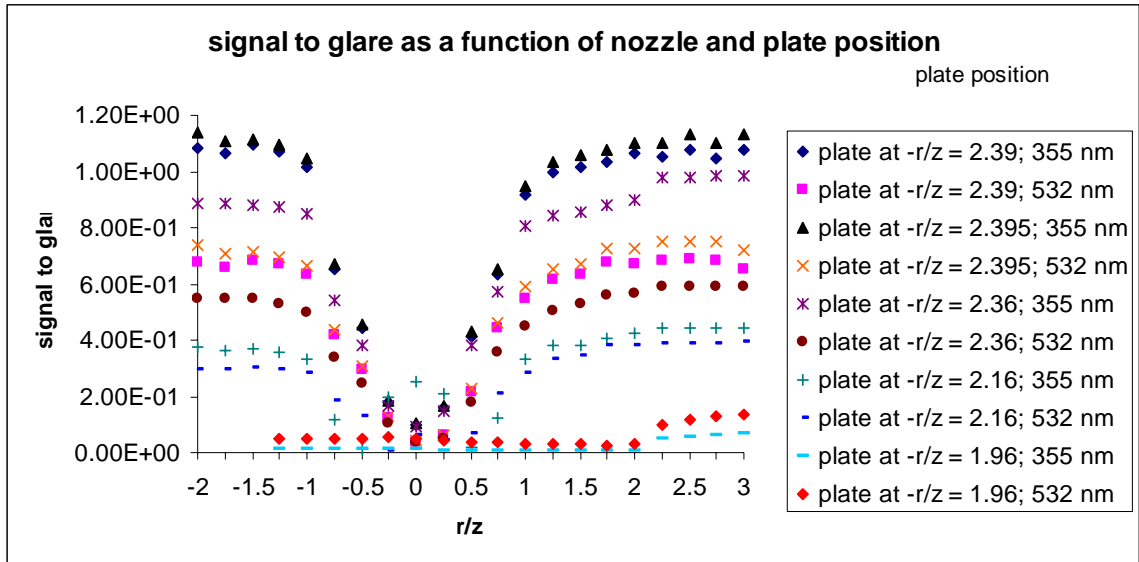


Figure 5-15. Signal-to-glare as a function of radial and plate position for 532 nm and 355 nm for a downstream location of 4 nozzle diameters and when a mixture of 20% helium and 80% nitrogen is flowing through the nozzle

It was observed that signal-to-glare ratio was higher outside the shear layer in the ambient and minimum at the jet center line. It was also seen that the signal-to-glare ratio is not symmetric about the jet center line. This was because the glare is higher when the nozzle was closer to the plate and gradually decreased as the nozzle was moved away from the nozzle. The lowest signal-to-glare ratio was observed when the plate was at 5 cm. It was seen that the hydrogen leak can be detected when the signal-to-glare ratio is as low as 0.166.

Detection limits

Figure 5-16 shows the raw peak voltage as a function of the radial position when there was no plate for 532 nm and 355 nm. These measurements were taken at nozzle position of 8 nozzle diameters downstream and when 100% helium was flowing through the nozzle. The Reynolds number was 100.

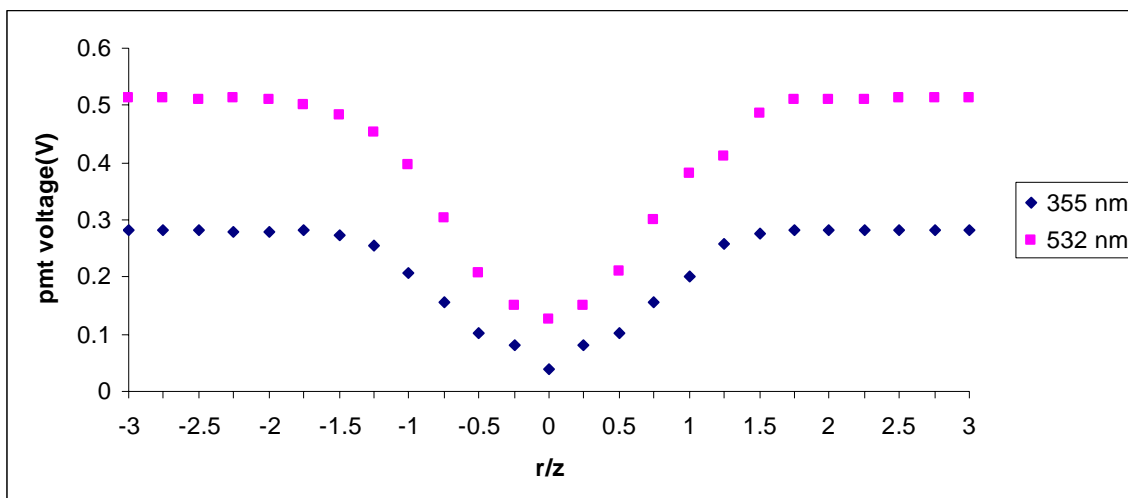


Figure 5-16. Raw photomultiplier-tube voltages as a function of radial and plate position for 532 nm and 355 nm at 8 nozzle diameters downstream and when 100% helium is flowing through the nozzle.

It was observed that the fall in voltage occurred over a wider range as compared to the nozzle position of 4 nozzle diameters downstream. This was because when the nozzle was at 8 nozzle diameters downstream, the jet spreads out and the variation in voltage due to the presence of helium occurred over a wider radius. The drop in voltage was around 15%.

To test for the detection limits, measurements were taken when the plate was placed as close as possible to the nozzle. Figure 5-17 shows the Rayleigh light scattering signal as a function of the radial position when the plate was at 5.5 cm from the nozzle for 532 nm. The measurements were taken at a nozzle position of 8 nozzle diameters downstream and when 100% helium was flowing through the nozzle. The Reynolds number was 100. To attenuate the intensity of the scattered beam a neutral density filter of optical density 0.6 was used.

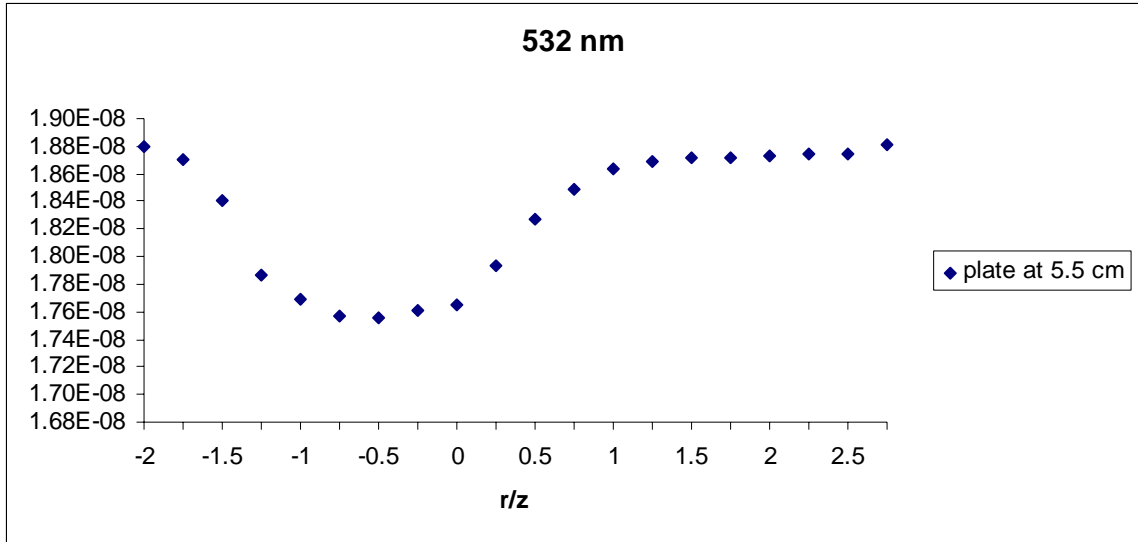


Figure 5-17. Rayleigh light scattering signal as a function of radial and plate position for 532 nm for a downstream location of 8 nozzle diameters and when 100% helium is flowing through the nozzle.

Figure 5-18 shows the Rayleigh light scattering signal as a function of the radial position when the plate was at 5.5 cm from the nozzle for 355 nm.

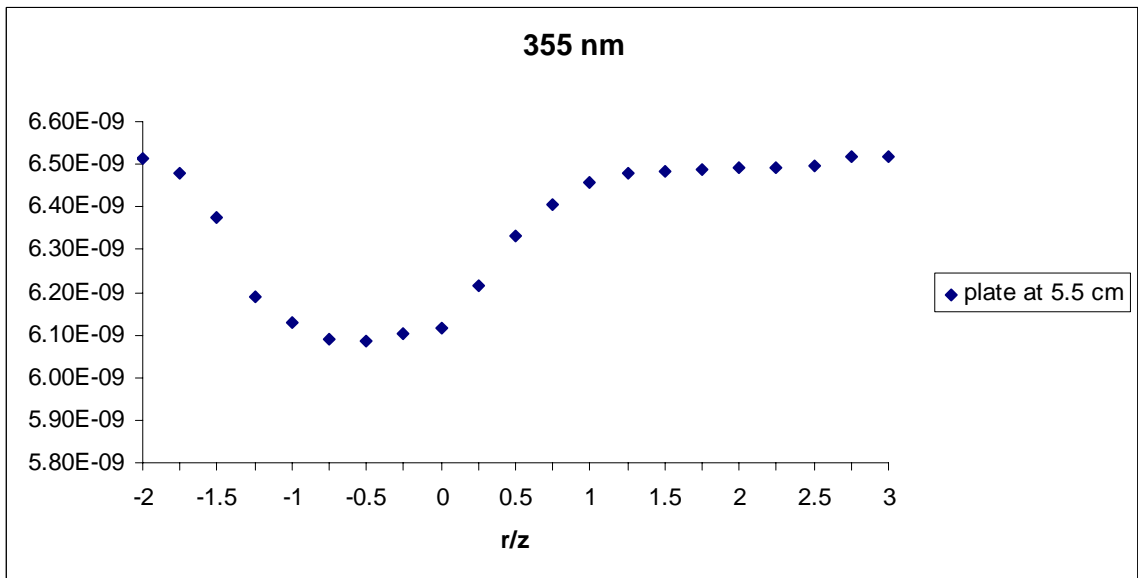


Figure 5-18. Rayleigh light scattering signal as a function of radial and plate position for 355 nm for a downstream location of 8 nozzle diameters and when 100% helium is flowing through the nozzle.

The glare here was eliminated by considering that the ratio of the glare at the two wavelengths was constant. From Figures 5-17 and 5-18, it was observed that there was a

fall in voltage at the jet centerline but the fall in voltage does not correspond to the ratio of the scattering cross-section of helium and air. This was because at 8 nozzle diameters, the jet spreads out and there will be greater entrainment of air. This caused the signal to be greater than expected since the scattering cross-section of air was greater than that of helium. The scattering cross-sections of air and helium are shown in Table 5-3.

Correlation studies

Figure 5-19 shows the correlation of Rayleigh light scattering signal between the two wavelengths: 355 nm and 532 nm when there was no plate, when the plate was at 6.083 cm, 6.08 cm, 6 cm and 5.5 cm from the nozzle.

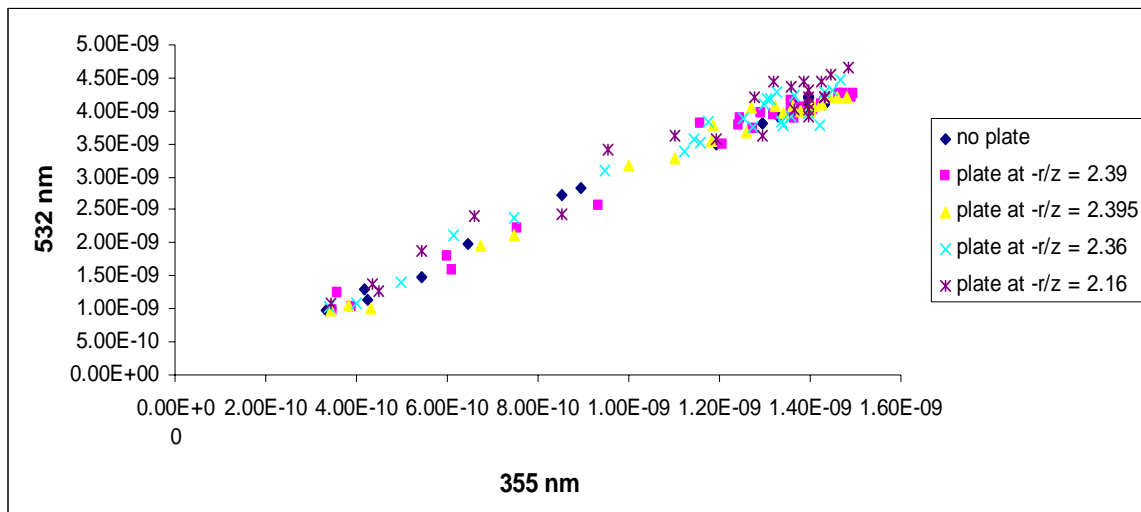


Figure 5-19. Correlation of Rayleigh light scattering signal between two wavelengths.

The correlation of the Rayleigh light scattering signals between the two wavelengths was drawn so that there are two sets of data to analyze and detect the hydrogen leak present in the jet. Figure 5-20 shows the R^2 value for the correlation of the Rayleigh light scattering signal at the two wavelengths as a function of the plate position. It was observed that the value of the correlation coefficient, R^2 is a minimum of 0.9567 when the plate is at 5.5 cm from the nozzle. Hence it was concluded that a decrease in

voltage on one line will imply a decrease in voltage on the second line as well. Hence there are two sets of data available and by analyzing the two sets of data simultaneously; it is possible to predict the presence of hydrogen leak in the jet.

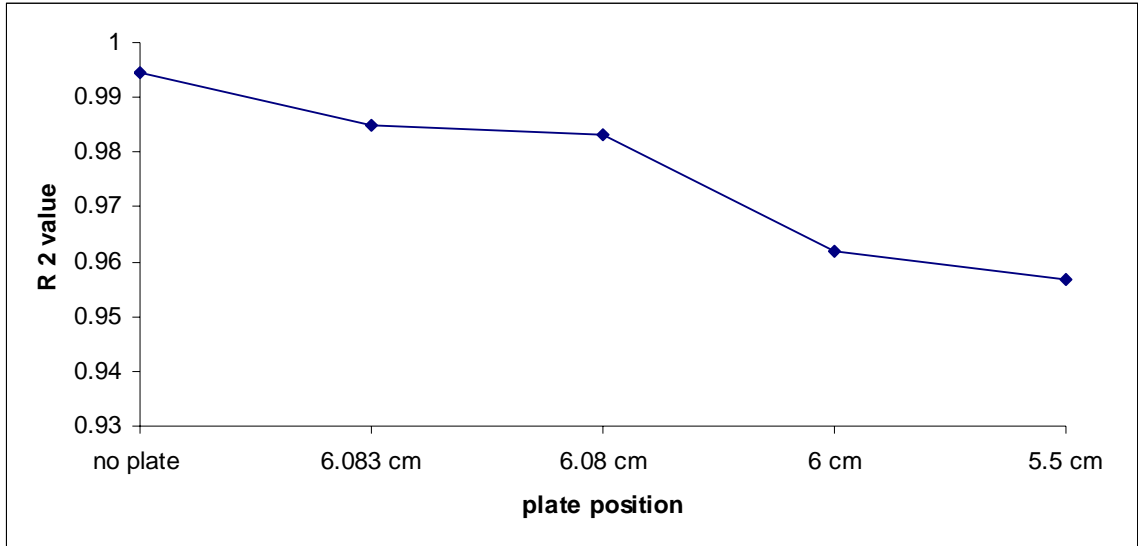


Figure 5-20. Variation in R² value as a function of plate position.

It was observed that the R² value for the correlation was highest and is equal to 0.9944 when there was no plate and gradually decreased as the plate was moved closer to the nozzle. So it was concluded that as the plate was moved closer to the nozzle, the uncertainty in the Rayleigh light scattering signal increased.

CHAPTER 6 CONCLUSIONS AND RECOMMENDATIONS

A Nd:YAG pulsed laser induced dual line-detection Rayleigh light scattering technique was used to detect the presence of hydrogen in the jet in the presence of high amounts of glare. Also, a mathematical code in MATLAB has been written to compute the glare numerically, design the experimental system and study the variation in the glare as a function of the plate position.

The MATLAB code computed only the glare from the aluminum plate and did not take into account the glare from the background surfaces. The results from the mathematical code are compared with experimental results by normalizing the glare and the results corresponded well. The percentage error between the numerical and experimental results was a maximum of 5%.

Two methods were used to eliminate the glare from the signal. When multiple surfaces are considered, glare from the signal is eliminated taking reference values at each point in space and when the glare from one surface is dominant compared to the glare from the other surfaces; the data analysis to eliminate the glare was simplified. The ratio of the glare at the two wavelengths is proved to be constant and the glare is eliminated by solving a set of simultaneous equations

Dual line-detection technique was used successfully to eliminate the glare from the signal and get accurate results even when the glare to signal ratio was as high as 6:1. When a mixture of 20% helium and 80% nitrogen was used for the measurements at 4 nozzle diameters, the voltage at the centerline of the nozzle was around 0.2 times that of

voltage outside the shear layer. This indicated a reduction in the scattering cross-section of the gas in the jet centerline by an amount of 0.2 as compared to the scattering cross-section of the gas outside the shear layers. This reduction in the scattering cross-section corresponded well to the ratio of the scattering cross-sections of hydrogen and air. The scattering cross-section of hydrogen is equal to 0.23 times that of air.

When pure helium was used for measurements at a downstream location of 8 nozzle diameters, a fall in voltage was observed in the centerline of the jet. The voltage at the jet centerline was observed to be 0.14 times that of the voltage outside the shear layers. The scattering cross-section of helium is equal to 0.015 times that of air. The decrease in the voltage at the jet centerline does not correspond well the ratio of the scattering cross-sections of helium and air. This is because at a downstream location of 8 nozzle diameters, the jet spreads out and there will be greater entrainment due to air.

Future work:

- A study should be done to eliminate the glare from the signal at downstream distances greater than 8 nozzle diameters and establish the detection limits.
- Also, a study should be done to detect the hydrogen leaks in the presence of cross currents.
- The feasibility of the technique should be determined in the back scatter mode to enable remote detection.

LIST OF REFERENCES

- Bohren, C. F., and Donald R. Huffman., Absorption and scattering of light by small particles, New York, John Wiley & Sons, 1983.
- Bryner, N., Richards, C.D., and Pitts, W.M., A Rayleigh Light Scattering Facility for the Investigation of Free Jets and Plumes, Review of Scientific Instruments, Vol. 63, No. 7, 3629-3635, 1992.
- Chen, C., Rodi W., The Science and Applications of Heat and Mass Transfer, HMT, 1980, Vol. 4.
- Dibble, R.W., Hollenbach, R.E., and Rambach, G.D., Laser Probes for Combustion Chemistry (ed. D.R. Crosley), 1980, Washington, DC, American Chemical Society, 435-441. Temperature measurements in turbulent flames via Rayleigh scattering,
- Dyer, T., Rayleigh scattering measurements of time resolved concentration in a turbulent propane jet, AIAA Journal, Vol. 17, No. 8, 1979, pp. 912-914.
- Geoff, A., Jason, K.B., Randall, J.K., and Paul, H., Raman and Rayleigh Holographic Lidar, Applied Optics, Vol. 41, No. 9, 2002, pp. 1798-1804.
- Graham, S., Grant, A., Jones, J., Transient molecular concentration measurements in turbulent flows using Rayleigh light scattering, AIAA Journal, Vol. 12, No. 8, 1974, pp. 1140-1142.
- Horton, J., Peterson, J.E., Transient temperature measurements in an ideal gas by using laser induced Rayleigh light scattering, Review of Scientific Instruments, Vol. 70, No. 8, 1999, pp. 3222-3226.
- Kerker, M. The Scattering of Light and Other Electromagnetic Radiation, New York, Academic Press, 1969.
- Long, M., Chu, B., and Chang, R., Instantaneous two dimensional gas concentration measurements by light scattering, AIAA Journal, Vol. 19, No. 9, 1981, pp. 1151-1157.
- Matthew, A., Peterson, J.E., Flow visualizations and transient temperature measurements in an axisymmetric impinging jet rapid thermal chemical vapor deposition reactor, Journal of Heat Transfer, Vol. 124, 2002, 564-570.
- McCartney, Earl J., Optics of the Atmosphere, New York, John Wiley & Sons, 1976.

- Muller-Dethlefs, K., Weinberg, F., Burning velocity measurements based on laser Rayleigh scattering, Seventeenth Symposium on Combustion, 1979, pp. 985-992.
- Namazian, N., Kelly J., Shefer, R.W., Johnston, S.C., and Long, M.B., Nonpremixed Bluff-Body Burner Flow and Flame Imaging Study, Experiments in Fluids, Vol. 8, 1989, pp. 216-228.
- Namer, I., and Schefer, R.W., Error Estimates for Rayleigh Scattering Density and Temperature Measurements in Premixed Flames, Experiments in Fluids Vol. 3, 1985, pp. 1-9.
- Otugen M.V., Annen, K.D., and Seasholtz, R.G., Gas Temperature Measurements Using a Dual-Line Detection Rayleigh Scattering Technique, AIAA Journal, Vol. 31, No. 11, 1993, pp. 2098-2104.
- Otugen M.V., Kim, J., and Popovic, S., Nd:YAG laser based dual line Rayleigh scattering system, AIAA Journal, Vol. 35, No. 5, 1997.
- Otugen, M. V., and Namer, I., Rayleigh Scattering Temperature Measurements in a Plane Turbulent Air Jet, Experiments in Fluids, Vol. 6, No. 7, 1988, pp. 461-466.
- Pitts, W.M., and Kashiwagi, T., The application of laser induced Rayleigh light scattering to the study of turbulent mixing, Journal of Fluid Mechanics, Vol. 141, 1983, pp. 391-429.
- Pitz, R.W., Cattolica, R., Robben, F., and Talbot, F., Temperature and Density in a Hydrogen Air Flame from Rayleigh scattering, Combustion and Flame, Vol. 27, 1976, pp. 313-320.
- Robben, F., Noise in the Measurements of Light with Photomultipliers, Applied Optics, Vol. 10, No. 4, 1971, pp. 776-796.
- Robben, F., Comparison of density and temperature using Raman scattering and Rayleigh scattering using combustion measurements in jet propulsion systems, Proceedings of a Project SQUID workshop, Purdue University, 1975, pp. 179-195.
- Rosenweig, R., Hottel, H., and Williams, G., Smoke scattered light measurements of turbulent concentration fluctuations, Chemical Engineering Science, Vol. 15, No. 1, 2, 1961, pp. 111-129.
- Schlichting, Boundary Layer Theory, McGraw Hill Series in Mechanical Engineering, 1979.
- Van de Hulst, H.C., Light Scattering by Small Particles, London, Chapman & Hall, 1957.
- Zhu, J.Y., So, R.M.C., Otugen, M.V., and Hwang, B.C., Some Measurements in Binary Gas Jet, Experiments in Fluids, Vol. 9, 1990, 273-284.

BIOGRAPHICAL SKETCH

Raghuram Vempati completed his undergraduate degree in mechanical engineering from Jawaharlal Nehru Technological University, India, in April 2002. He is pursuing his master's degree in mechanical engineering at the University of Florida. He has been a research assistant under Dr. Jill Peterson since August 2002.